PHILOSOPHICAL TRANSACTIONS OF THE ROYAL SOCIETY A MATHEMATICAL, PHYSICAL & ENGINEERING SCIENCES

A Linear Stratified Ocean Model of the Equatorial Undercurrent

J. P. McCreary

Phil. Trans. R. Soc. Lond. A 1981 **298**, 603-635
doi: 10.1098/rsta.1981.0002

A LINEAR STRATIFIED OCEAN MODEL OF THE EQUATORIAL UNDERCURRENT

By J. P. McCREARY

Ocean Sciences Center, Nova University, 8000 North Ocean Drive, Dania, Florida 33004, *U.S.A.*

(*Communicated by Sir James Lighthill, F.R.S.* – *Received* 12 *July* 1979 – *Revised* 6 *February* 1980)

CONTENTS

A linear stratified ocean model is used to study the wind-driven response of the equatorial ocean. The model is an extension of the Lighthill (1969) model that allows the diffusion of heat and momentum into the deeper ocean, and so can develop non-trivial steady solutions. To retain the ability to expand solutions into sums of vertical normal modes, mixing coefficients must be inversely proportional to the square of the back-

 [Published 21 January 1981

ground Väisälä frequency. The model is also similar to the earlier homogeneous ocean model of Stommel (1960). He extended Ekman dynamics to the equator by allowing his model to generate a barotropic pressure field. The present model differs in that the presence of stratification allows the generation of a baroclinic pressure field as well.

The most important result of this paper is that linear theory can produce a realistic equatorial current structure. The model Undercurrent has a reasonable width and depth scale. There is westward flow both above and below the Undercurrent. The meridional circulation conforms to the 'classical' picture suggested by Cromwell (1953). Unlike the Stommel solution, the response here is less sensitive to variations of parameters. Ocean boundaries are not necessary for the existence of the Undercurrent but are necessary for the existence of the deeper Equatorial Intermediate Current.

The radiation of equatorially trapped Rossby and Kelvin waves is essential to the development of a realistic Undercurrent. Because the system supports the existence of these waves, low-order vertical modes can very nearly adjust to Sverdrup balance (defined below), which in a bounded ocean and for winds without curl is a state of rest. As a result, higher-order vertical modes are much more visible in the total solution. This property accounts for the surface trapping and narrow width scale of the equatorial currents. The high-order modes tend to be in Yoshida balance (defined below) and generate the characteristic meridional circulation pattern associated with equatorial Ekman pumping.

1. Introduction

The Pacific Equatorial Undercurrent was rediscovered in August 1952 (Cromwell *et al.* 1954) and immediately captured the attention of the oceanographic community. Similar currents have since been found in the Atlantic and Indian Oceans as well, and a bewildering variety of explanations have been proposed to account for the phenomenon. The papers discussed below provide only background information pertinent to the present study. An extensive survey of the relevant literature, both observational and theoretical, can be found in Philander (1973). Gill (1972) and Moore & Philander (1978) review various models of equatorial ocean circulation with application to the Undercurrent.

(*a*) *Observational background*

An example of the Undercurrent from the equatorial Atlantic, which summarizes many of its familiar characteristics, is given in figure 1. The current appears as a region of geostrophically balanced eastward flow located in the strong pycnocline beneath the surface mixed layer. It is confined within 200 km of the equator, is about 100 m thick, and reaches speeds in excess of 120 cm/s. The meridional circulation associated with this jet can be inferred from the temperature data. The spreading of isotherms suggests that there is upwelling above and downwelling at and below the core of the Undercurrent; conservation of mass then requires divergence of water from the equator at the ocean surface and convergence of water slightly above the current core. Knauss (1966) has estimated the magnitude of the convergence and upwelling (in the Pacific Ocean) to be 1–10 cm/s and $0.5–5 \times 10^{-3}$ cm/s, respectively.

The Undercurrent is usually found sandwiched between westward flows (Philander 1973). The surface drift typically has speeds of the order of 50 cm/s but can vary considerably in strength. Occasionally there is no westward surface flow at all (Jones 1969). Westward flow beneath the Undercurrent, the Equatorial Intermediate Current, can extend to depths of 1200 m and can have speeds as large as 40 cm/s.

When the Undercurrent is well developed the strong near-surface pycnocline and also the

current core shoal toward the east. The shoaling of the pycnocline replaces a thick, well mixed surface layer in the western ocean with a deeper, relatively homogeneous layer, the thermostad, in the eastern ocean (see, for example, Philander 1973, figure 7). With a level of no motion at greater depths, the surface dynamic-height field must slope downward toward the east. It follows that the near-surface waters, including the Undercurrent, experience an eastward pressure force. In the central Pacific the downward slope of the sea surface is roughly -5×10^{-8}, equivalent to a pressure gradient force ($-\bar{\rho}^{-1}p_x$) of 5×10^{-5} dyn†/g; at the depth of the current core the pressure gradient force decreases to a value of 2.6×10^{-5} dyn/g (Knauss 1966).

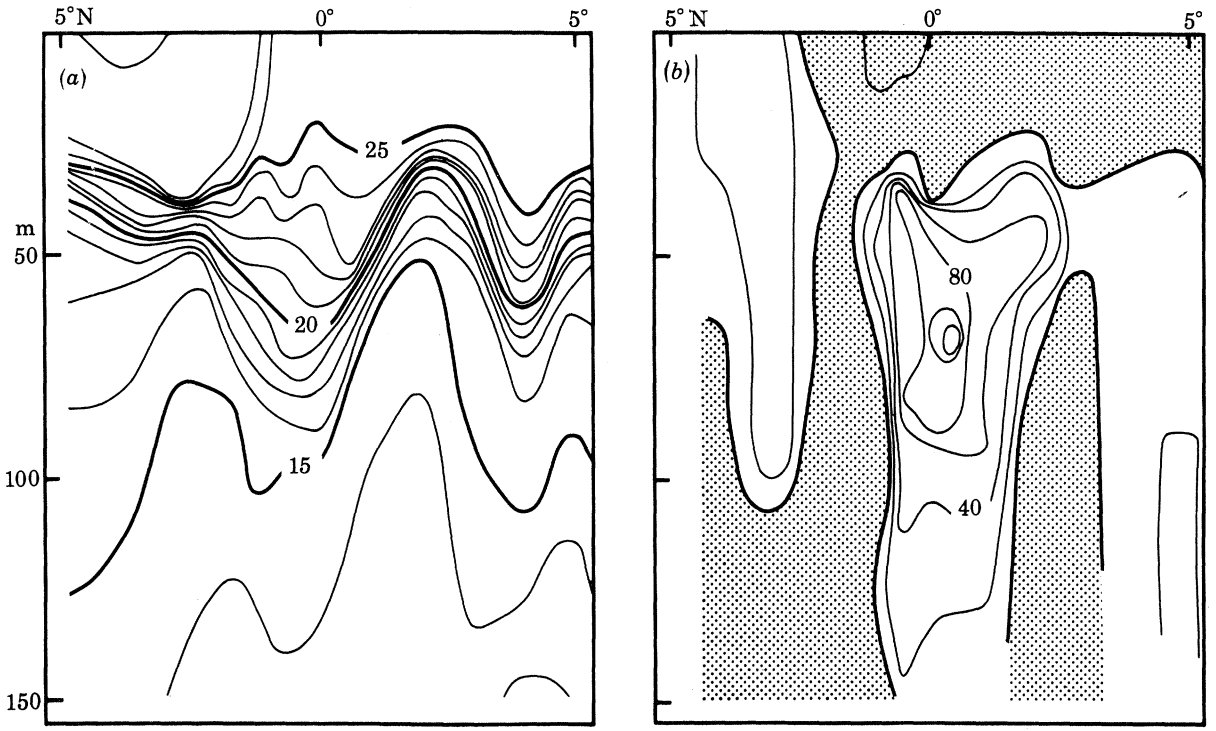

FIGURE 1. An example of the Atlantic Equatorial Undercurrent at 5° W in January 1975: (*a*) Temperature/°C and (*b*) zonal velocity/(cm/s) as a function of latitude and depth. The unmarked contour at the core of the Undercurrent is 120 cm/s. After Moore *et al.* (1978).

Recent observations suggest that the equatorial current structure is more complicated than the classical description of the preceding paragraphs would suggest; for example, the Undercurrent meanders (Duing *et al.* 1975). At the base of the well developed surface mixed layer in the western Pacific a secondary ageostrophic eastward current has been observed (Hisard *et al.* 1970). Beneath the Undercurrent, flow need not be entirely westward but can consist of a set of stacked zonal jets (Luyten & Swallow 1976; C. C. Eriksen 1979 private communication). In the eastern Pacific and elsewhere subsurface eastward jets, distinct from the Undercurrent and Countercurrent, have been observed a few degrees from the equator; these jets are associated with the poleward limits of the thermostad (Tsuchiya 1975).

† dyn = 10^{-5} N.

(*b*) *Theoretical background*

In nearly all explanations of the Undercurrent it is assumed that the primary driving mechanism is the easterly tradewinds. These explanations are based on the following physically motivated ideas. At the equator the trades force a westward drift. Water piles up in the western ocean and so generates an eastward pressure force near the surface (Montgomery & Palmén 1940). This force then provides the source of momentum to drive the Undercurrent (Arthur 1960). A heuristic application of mid-latitude Ekman theory near the equator suggests that the trades must also force a surface divergence of water at the equator and so create upwelling and deeper convergence there (Cromwell 1953).

Stommel (1960) was the first to incorporate these ideas in a mathematical model. His momentum equations balanced the Coriolis force with the vertical diffusion of momentum (the Ekman balance) but also retained pressure gradients. Since his model ocean was unstratified, the pressure field was necessarily barotropic. It is the presence of these pressure gradients that prevents the equatorial singularity of Ekman flow. The Stommel model is the simplest way to extend Ekman dynamics to the equatorial region in a homogeneous ocean.

Stommel's solution depends strongly on the depth of the ocean. If it is applied to the entire water column, there is a very poor comparison with observation (see, for example, discussion of equations (51) and figure 9). For a realistic choice of eddy viscosity the currents are far too large and far too narrow. Moreover, the subsurface flow is not surface-trapped, but extends to the ocean bottom. If the solution is applied to a surface mixed layer about 100 m thick, there is much better agreement, and many of the qualitative features described above are present in the solution. Even in this case, however, the model has major limitations. It is not possible to choose a value for eddy viscosity that simultaneously sets a realistic magnitude as well as a width scale for the flow. Finally, the model Undercurrent is ageostrophic, and, by assumption, lies entirely in the surface mixed layer.

Evidently Stommel's dynamics neglect physical processes that are important near the equator. A number of other studies of thin homogeneous layers have examined the effects of terms neglected in Stommel's equations (particularly the nonlinear terms) and do manage to avoid some of the difficulties inherent in this solution (Charney 1960; Robinson 1966; Charney & Spiegel 1971; Gill 1971; McKee 1973; Cane 1979). Nevertheless, because the actual Undercurrent lies predominantly in the thermocline, it seems likely that stratification (necessarily ignored in the layer models) must play an essential role in its dynamics.

The importance of stratification was illustrated in a simple way by Arthur (1960). He considered the same linear equatorial balance of terms as did Stommel (that is, an equatorial balance between the vertical diffusion of momentum and the pressure gradient force) but, because his model ocean was stratified, he allowed the pressure field to have a baroclinic component. He then assumed a pressure field similar to that observed and calculated the resulting equatorial current structure over the entire water column. For reasonable values of eddy viscosity, the flows have realistic magnitudes; moreover, they are strongly trapped near the surface! The unsatisfying aspect of this calculation is that the pressure field is set by assumption. In an adequate theory of the Undercurrent, the baroclinic pressure field must emerge as a result of the solution of the equations of motion.

Lighthill (1969) popularized the study of a linear stratified model that does internally generate its own baroclinic pressure field. He dropped nearly all nonlinear terms from the governing

equations but retained the effects of the vertical advection of density by linearizing that term about a background density state. Wind stress enters the ocean as a body force in a surface mixed layer, and the deeper ocean is inviscid. The advantages of the Lighthill formulation are enormous, both mathematically and conceptually. Solutions are expressed as sums over all possible vertical normal modes allowed by the system, and in this way three-dimensional dynamics reduce to a set of two-dimensional equations. The time-dependent response of each mode is conveniently described in terms of the propagation of equatorially trapped waves. There is a natural width scale for equatorial phenomena, the baroclinic equatorial Rossby radius of each mode. Further discussions of this model can be found in Moore & Philander (1978), Cane & Sarachik (1976, 1977) and McCreary (1977).

The Lighthill model has had considerable success in describing transient ocean phenomena (Lighthill 1969; Anderson & Rowlands 1976; McCreary 1976, 1977). In fact, Gill (1972) has used the approach to study the initial spin-up of the Undercurrent from a quiescent ocean. However, the model cannot describe the observed steady equatorial current structure. In the steady state, flow is entirely in the surface mixed layer, and if the driving winds have no curl there is no flow at all (see the discussion of equations (53)). The success of the Arthur calculation suggests that this failure may occur not because of the neglect of nonlinearities, but rather because the deeper ocean in Lighthill's model is inviscid. As a result, there is no way for momentum or heat to diffuse into or out of the surface mixed layer.

Recently, Semtner & Holland (1980), and also Philander & Pacanowski (1980), have studied fully three-dimensional, nonlinear, stratified ocean models. These models are remarkably successful in reproducing many of the observed features of the Undercurrent. However, as is often the case with complicated numerical models, it is difficult to determine the dominant processes at work in them. Important questions remain unanswered in both of these studies. What mechanisms adjust the width and depth scales of their solutions? How is the baroclinic pressure field established? What role do equatorially trapped Rossby and Kelvin waves play in the models? Most importantly, are nonlinearities (other than the vertical advection of density) in fact necessary for the generation of the Undercurrent?

(*c*) *The present approach*

This paper continues the effort to relate the easterly tradewinds to the presence of the Equatorial Undercurrent. Specifically, the effects of stratification on the steady equatorial circulation are investigated. The model developed here is an extension of Lighthill's (1969) model that allows the diffusion of heat and momentum into the deeper ocean but at the same time retains all the advantages of Lighthill's approach. In particular, by choosing depth-dependent diffusion coefficients of a specific form, solutions can still be represented as sums over vertical normal modes.

The simplicity of the model allows a discussion of its dynamics in a novel way and suggests answers to the questions posed above. For example, there is a close connection between the radiation of equatorially trapped Rossby and Kelvin waves and the steady solutions found here, and that relationship is exploited throughout. The linear model is able to account for many of the observed features of equatorial current structure. This success suggests that the neglected nonlinearities are not essential for the existence of the Undercurrent.

2. The model ocean

(a) *Equations and assumptions*

In a state of no motion the model ocean has a stably stratified background density structure $\rho_b(z)$ and an associated Väisälä frequency $N_b(z)$. Model equations linearized about this background state are

$$\left.\begin{aligned} u_t - fv + p_x &= (\nu u_z)_z, \\ v_t + fu + p_y &= (\nu v_z)_z, \\ u_x + v_y + w_z &= 0, \\ \rho_t - g^{-1}N_b^2 w &= (\kappa\rho)_{zz}, \\ p_z &= -\rho g, \end{aligned}\right\} \tag{1}$$

where u, v, and w are the zonal, meridional and vertical velocity anomalies, respectively, p and ρ are the pressure and density anomalies, g is the acceleration due to gravity, f is the Coriolis parameter, and ν and κ are coefficients of eddy viscosity and eddy diffusivity. Constant factors of $\bar{\rho}$, the average density of the water column, are everywhere ignored. The equatorial β-plane is assumed; that is, $f = \beta y$. A comprehensive study of similar linear sets of equations can be found in Veronis (1973), or Moore & Philander (1978).

Throughout this paper, eddy coefficients are assumed to be inversely proportional to N_b^2, that is,

$$\nu = A/N_b^2, \quad \kappa = A/N_b^2; \tag{2}$$

moreover, as is evident in (1), the diffusion of heat and the diffusion of momentum have slightly different forms. These choices are crucial to the entire approach taken here. Only in this way is it still possible to find solutions, as Lighthill did, as expansions of vertical normal modes. Previous workers have already recognized the mathematical convenience of these forms of vertical mixing; Fjeldstad (1963), and later Mork (1972), used them in their internal wave studies. Another assumption is that the constant of proportionality, A, is the same for both ν and κ, and it effectively sets the Prandtl number to unity. This restriction is not essential to any of the mathematical procedures discussed below, and can be relaxed if desired.

Surface boundary conditions, at $z = 0$, are

$$\nu u_z = \tau^x, \quad \nu v_z = \tau^y, \quad w = \rho/N_b^2 = 0, \tag{3}$$

where τ^x and τ^y are the zonal and meridional components of wind stress acting at the ocean surface. The ocean bottom, at $z = -D$, is flat. Bottom boundary conditions are

$$\nu u_z = \nu v_z = w = \rho/N_b^2 = 0. \tag{4}$$

Requiring that $\rho/N_b^2 = 0$ at ocean boundaries means that both the atmosphere and the ocean bottom act as constant-temperature sources of heat. The condition of zero stress at the bottom assumes that the bottom is very slippery. This assumption might be worrisome if solutions developed large bottom currents, but, as we shall see, the currents are strongly surface-trapped. If $N_b(z)$ changes discontinuously at some level in the water column, at $z = -H$, then equations (1) require that

$$u,\ v,\ p,\ w,\ \rho/N_b^2,\ \nu u_z, \nu v_z \text{ and } (\kappa\rho)_z \quad \text{are continuous} \tag{5}$$

across the interface.

(b) *Barotropic and baroclinic modes*

Because of the specific form for eddy coefficients and boundary conditions, solutions to (1) can be expressed in terms of the eigenfunctions $\psi_n(z)$, where each ψ_n satisfies

$$\psi_{nz} = -\frac{N_b^2}{c_n^2}\int_{-D}^{z} \psi_n \, dz, \tag{6}$$

subject to the condition $$\frac{1}{c_n^2}\int_{-D}^{0}\psi_n\,dz = 0. \tag{7}$$

If there is a discontinuity of N_b at $z = -H$, (6) is solved so that

$$\psi_n(z) \quad \text{is continuous} \tag{8}$$

across the interface. The eigenfunctions are the vertical normal modes of the system and form an orthogonal set. They are commonly normalized so that

$$\psi_n(0) = 1. \tag{9}$$

It is convenient to order them so that the eigenvalues c_n decrease monotonically with n. In that case as $n \to \infty$, $c_n \to \text{const.} \times n^{-1}$.

The solutions to (1), subject to the boundary conditions (3)–(5), can then be written

$$\left.\begin{aligned} u = \sum_{n=1}^{N} u_n\psi_n, \quad v = \sum_{n=1}^{N} v_n\psi_n, \quad p = \sum_{n=1}^{N} p_n\psi_n, \\ w = \sum_{n=1}^{N} w_n\int_{-D}^{z}\psi_n\,dz, \quad \rho = \sum_{n=1}^{N}\rho_n\psi_{nz}, \end{aligned}\right\} \tag{10}$$

where the expansion coefficients u_n, v_n, p_n, w_n and ρ_n are functions only of x, y and t. There are standard techniques for finding the equations governing the expansion coefficients. The equations are

$$\left.\begin{aligned} \left(\partial_t + \frac{A}{c_n^2}\right)u_n - fv_n + p_{nx} &= F_n, \\ \left(\partial_t + \frac{A}{c_n^2}\right)v_n + fu_n + p_{ny} &= G_n, \\ \left(\partial_t + \frac{A}{c_n^2}\right)\frac{p_n}{c_n^2} + u_{nx} + v_{ny} &= 0, \\ w_n = \left(\partial_t + \frac{A}{c_n^2}\right)\frac{p_n}{c_n^2}, \quad \rho_n &= -\frac{p_n}{g}, \end{aligned}\right\} \tag{11}$$

where $$F_n = \tau^x \Big/ \int_{-D}^{0}\psi_n^2\,dz, \quad G_n = \tau^y \Big/ \int_{-D}^{0}\psi_n^2\,dz. \tag{12}$$

F_n and G_n measure how well each mode couples to the driving wind.

The $n = 0$ eigenfunction is distinctly different from the others. Equations (6), (7), and (8) have a solution when $c_0 = \infty$. The form of this eigenfunction is simply

$$\psi_0(z) = 1, \tag{13}$$

which is the barotropic mode of the system. The eigenfunctions for $n \geqslant 1$ have finite eigenvalues. To satisfy (7) the eigenfunctions must now meet the condition

$$\int_{-D}^{0}\psi_n(z)\,dz = 0. \tag{14}$$

Since u_n and v_n are both proportional to $\psi_n(z)$, (14) implies that horizontal transport vanishes for these modes. They are the baroclinic modes of the system.

Equations (11) reduce to a simple form for the barotropic mode. Since $c_0 \to \infty$, terms involving c_0 can be ignored. Therefore, steady barotropic flow is in Sverdrup balance and requires the

existence of wind stress curl. If the wind has no curl there are no barotropic currents; rather, a pressure gradient force (that is, a sea level slope) everywhere balances the wind stress. The solutions of this paper are driven by steady winds with weak curl, and the barotropic mode does not significantly affect the currents. For this reason it is ignored in the remainder of this paper, and the sums in (10) begin at $n = 1$.

In theory there are an infinite number of baroclinic eigenfunctions that must be included in the sums (10). In practice, the upper limit of the sums is necessarily a finite value, N. So, this method of solution will be of value only if the series converge rapidly enough with n, so that N need not be too large. As we shall see, for realistic choices of $\rho_b(z)$ and ν, rapid convergence is ensured.

(c) *A surface mixed layer*

It is possible to incorporate a constant-thickness surface mixed layer into the model simply by assuming that $N_b(z) = 0$ for $z > -H$. The eigenfunction problem, as defined in (6)–(8), is still well posed, and so the eigenfunctions as well as the solutions (10) remain well behaved. (Strictly speaking, since factors of N_b^2 appear in the denominators of several quantities, one must first take $N_b(z) = \epsilon$ for $z > -H$, find the solutions (10), and then determine the limit $\epsilon \to 0$.)

The dominant effect of the mixed layer on the eigenfunctions is that

$$\psi_{nz} = 0, \quad z > -H. \tag{15}$$

Therefore, in the mixed layer, u, v, and p are independent of z, w varies linearly with z, and $\rho \equiv 0$. Stress, defined by

$$\boldsymbol{\tau} = \lim_{\epsilon \to 0} \nu \boldsymbol{u}_z, \tag{16}$$

varies linearly throughout the layer, from a surface value set by the wind, to a value at $z = -H$ set by the deeper ocean. In effect, wind stress acts as a depth-independent body force throughout the layer. Heat flux, defined by

$$Q = \lim_{\epsilon \to 0} (\kappa \rho)_z, \tag{17}$$

is constant throughout the layer. So whatever heat is absorbed (lost) at the base of the layer is instantly lost (absorbed) at the surface. The mixing coefficients, ν and κ, are very large (infinite) in the layer. These properties are all to be expected in a very well mixed surface layer.

The model does allow both upwelling and downwelling of fluid from the mixed layer. Upwelling occurs in a sensible way, but downwelling does not. When a water particle upwells into the layer its density anomaly ρ instantly becomes zero. The model provides a mechanism that can account for this density jump, since mixing is so strong that the water particle is essentially always in contact with the atmosphere, where $\rho = 0$. When a water particle downwells, ρ changes instantly from zero to some value that is not necessarily zero. There is no corresponding mechanism that can create this jump, because mixing coefficients have a finite value in the deep ocean.

A related difficulty inherent in this mixed layer formulation is that ρ is not necessarily positive just beneath the interface, and it is possible for the model to generate density inversions there. According to (10) and (11), in steady state w and ρ have the same sign just beneath the interface. (This property follows because for all n, $\int_{-D}^{z} \psi_n \, dz < 0$, and $\psi_{nz} > 0$ there.) Consequently, upwelling produces a stably stratified density jump across the interface, but downwelling necessarily produces a density inversion.

With the presence of this surface mixed layer the model is very similar to Lighthill's model. The sole difference is that, since his deep ocean is inviscid, his linear stress profile in the mixed layer vanishes at $z = -H$. Equations (11) reduce to Lighthill's equations when $A \equiv 0$.

3. The solution

To evaluate the solutions (10) it is necessary to determine the expansion coefficients u_n, v_n and p_n that satisfy (11). Solutions to (11) are difficult to find for winds that depend arbitrarily on x, y and t. So, in this section solutions are found for a wind field with the separable form

$$\tau^x = \tau_0 X(x)\, Y(y)\, e^{i\sigma t}, \quad \tau^y = 0. \tag{18}$$

The coupling coefficients, (12), are then given by

$$\left.\begin{aligned} F_n &= \tau_0 X(x)\, Y(y)\, e^{i\sigma t} \Big/ \int_{-D}^{0} \psi_n^2 \, dz \equiv \tau_{0n} X(x)\, Y(y)\, e^{i\sigma t}, \\ G_n &= 0, \end{aligned}\right\} \tag{19}$$

where τ_{0n} is defined in an obvious manner. $X(x)$ and $Y(y)$ are arbitrary functions, in which $Y(y)$ weakens away from the equator, and $X(x)$ is non-zero only in a region of finite extent; hence the model is forced by a patch of wind confined to the ocean interior. Meridional winds are ignored since they are not necessary for the existence of the Equatorial Undercurrent. To illustrate more clearly how the effects of radiation enter into the solution, it is useful first to find the model response to oscillatory winds. The response of the model to a steady wind is found simply by setting $\sigma = 0$ everywhere in the resulting solution.

Solutions are found for unbounded, as well as bounded, oceans. When boundaries exist they are simple vertical barriers located at the positions $x = x_0, x_1$ and separated by the distance $d = x_1 - x_0$; northern and southern boundaries are ignored. There can be no flow across these barriers, so in the bounded ocean basin the solutions must satisfy the boundary conditions

$$u_n = 0 \quad \text{at} \quad x = x_0, x_1. \tag{20}$$

Nearly all the quantities involved in the following discussion depend in some way on the eigenvalue c_n, and for that reason they should be labelled with a subscript n (the exceptions are f, σ, X, Y, and β). For notational simplicity, this subscript will be deleted unless confusion might result from its absence. For the same reason, factors of $e^{i\sigma t}$ are ignored until the end of the derivation.

(a) *The Hermite functions*

Because $f = \beta y$ solutions can be expressed as sums of Hermite functions, ϕ_m, which satisfy

$$\phi_{myy} - (f^2/c^2)\,\phi_m = -\alpha_m^2 \phi_m, \tag{21}$$

and decay at high latitudes. One representation of these functions is

$$\phi_m(\eta) = \frac{(-1)^m}{[2^m m!\, \pi^{\frac{1}{2}}]^{\frac{1}{2}}} e^{\frac{1}{2}\eta^2} \frac{d^m}{d\eta^m} e^{-\eta^2}, \tag{22}$$

where

$$\left.\begin{aligned} \alpha_m^2 &= \alpha_0^2(2m+1), \quad m = 0, 1, 2, \ldots, \\ \alpha_0^2 &= \beta/c, \quad \eta = \alpha_0 y. \end{aligned}\right\} \tag{23}$$

Recursion relations, which follow immediately from (22), are

$$\left.\begin{aligned} \eta\phi_m &= \tfrac{1}{\sqrt{2}}(m+1)^{\frac{1}{2}}\phi_{m+1} + \tfrac{1}{\sqrt{2}} m^{\frac{1}{2}} \phi_{m-1}, \\ \phi_{m\eta} &= -\tfrac{1}{\sqrt{2}}(m+1)^{\frac{1}{2}}\phi_{m+1} + \tfrac{1}{\sqrt{2}} m^{\frac{1}{2}} \phi_{m-1}. \end{aligned}\right\} \tag{24}$$

Let q_m, $[\eta q]_m$ and $[q_\eta]_m$ be the Hermite coefficients of the functions $q(\eta)$, ηq, and q_η, respectively. Then, with the aid of (24),

$$\left.\begin{aligned}[\eta q]_m &= \tfrac{1}{\sqrt{2}}(m+1)^{\frac{1}{2}}\, q_{m+1} + \tfrac{1}{\sqrt{2}} m^{\frac{1}{2}}\, q_{m-1},\\ [q_\eta]_m &= \tfrac{1}{\sqrt{2}}(m+1)^{\frac{1}{2}}\, q_{m+1} - \tfrac{1}{\sqrt{2}} m^{\frac{1}{2}}\, q_{m-1}.\end{aligned}\right\} \tag{25}$$

It follows from (23) that a characteristic width scale for these functions is α_0^{-1}. This distance defines the equatorial Rossby radius of deformation for each vertical mode, and solutions involving these functions generally have some aspects that reflect this scale. Because of the dependence on c, α_0^{-1} decreases with increasing n. In fact, as $n \to \infty$, $\alpha_0^{-1} = \text{const.} \times n^{-\frac{1}{2}}$.

(*b*) *The unbounded response*

Elimination of u_n and p_n from (11) gives

$$v_{xx} + v_{yy} - \frac{f^2}{c^2} v + \frac{\omega^2}{c^2} v + \frac{\beta}{\mathrm{i}\omega} v_x = \frac{f}{c^2} F - \frac{1}{\mathrm{i}\omega} F_{yx}, \tag{26}$$

where

$$\omega = \sigma - \mathrm{i}A/c^2. \tag{27}$$

Let v_m and Y_m be the Hermite expansion coefficients of v_n and Y. Then these coefficients satisfy

$$v_{mxx} + \frac{\beta}{\mathrm{i}\omega} v_{mx} - \left(\alpha_m^2 - \frac{\omega^2}{c^2}\right) v_m = \tau_{0n}\alpha_0 \left(\frac{1}{c}[\eta Y]_m X - \frac{1}{\mathrm{i}\omega}[Y_\eta]_m X_x\right). \tag{28}$$

Equation (28) is an ordinary differential equation in x, and the method of Fourier transforms provides a straightforward method of solution. Designate the transform of a variable $q(x)$ by $\tilde{q}(k)$. Then,

$$\tilde{v}_m = -\tau_{0n}\alpha_0 \frac{(1/c)\,[\eta Y]_m - (k/\omega)\,[Y_\eta]_m}{(k-k_1^m)\,(k-k_2^m)} \tilde{X}, \tag{29}$$

where

$$k_{1,2}^m = \frac{\beta}{2\omega}\left\{1 \mp \left[1 - 4\frac{\omega^2}{\beta^2}\left(\alpha_m^2 - \frac{\omega^2}{c^2}\right)\right]^{\frac{1}{2}}\right\}. \tag{30}$$

Expanding (29) into partial fractions gives

$$\tilde{v}_m = -\sum_{j=1}^{2} P_j^m \frac{\tilde{X}}{k - k_j^m}, \tag{31}$$

where

$$P_j^m = \tau_{0n}\alpha_0 \frac{(1/c)\,[\eta Y]_m - (k_j^m/\omega)\,[Y_\eta]_m}{k_j^m - k_{j'}^m}, \tag{32}$$

and $j' \neq j$. The inverse Fourier transform of (31) is

$$v_m(x) = -\mathrm{i}\sum_{j=1}^{2} P_j^m \int_{L_j}^{x} \mathrm{e}^{-\mathrm{i}k_j^m x} X \,\mathrm{d}x\, \mathrm{e}^{\mathrm{i}(k_j^m x + \sigma t)}, \tag{33}$$

where

$$L_1, L_2 = \pm\infty. \tag{34}$$

The lower limits, L_j, are not specified in taking the inverse Fourier transform of (31). Rather, they must be chosen to satisfy appropriate radiation conditions. This point is discussed later in this section.

Elimination of p_n from the first and third equations of (11) gives

$$-\left(\partial_{xx} + \frac{\omega^2}{c^2}\right) u = \mathrm{i}\frac{\omega}{c^2} f v + v_{yx} + \mathrm{i}\frac{\omega}{c^2} F. \tag{35}$$

PHILOSOPHICAL TRANSACTIONS OF THE ROYAL SOCIETY A MATHEMATICAL, PHYSICAL & ENGINEERING SCIENCES

Let u_m be the set of Hermite expansion coefficients of u_n. Then these coefficients must satisfy

$$-\left(\partial_{xx}+\frac{\omega^2}{c^2}\right)u_m = \mathrm{i}\frac{\omega}{c}\alpha_0[\eta v]_m+\alpha_0[v_\eta]_{mx}+\mathrm{i}\frac{\omega}{c^2}F_m. \tag{36}$$

With the aid of (25), $\tilde{u}_m$ is given by

$$\tilde{u}_m = \mathrm{i}\alpha_0\left[\tfrac{1}{\sqrt{2}}(m+1)^{\frac{1}{2}}\frac{\tilde{v}_{m+1}}{k-\omega/c}-\tfrac{1}{\sqrt{2}}m^{\frac{1}{2}}\frac{\tilde{v}_{m-1}}{k+\omega/c}\right]+\mathrm{i}\frac{\omega}{c^2}\frac{\tilde{F}_m}{(k-\omega/c)\,(k+\omega/c)}. \tag{37}$$

Just as before, the solution proceeds by expanding (37) into partial fractions and then inverting each term. Some algebra, again with the aid of (25), shows that all except one of the terms with denominators $k\pm\omega/c$ vanish. The inverse Fourier transform of (37) reduces to

$$\begin{aligned} u_m(x) &= \tfrac{1}{\sqrt{2}}(m+1)^{\frac{1}{2}}R+\tfrac{1}{\sqrt{2}}m^{\frac{1}{2}}S+\delta_{m0}\,T \\ &= \tfrac{1}{\sqrt{2}}\alpha_0\,(m+1)^{\frac{1}{2}}\sum_{j=1}^{2}\frac{P_j^{m+1}}{k_j^{m+1}-\omega/c}\int_{L_j}^{x}\mathrm{e}^{-\mathrm{i}k_j^{m+1}x}\,X\,\mathrm{d}x\,\mathrm{e}^{\mathrm{i}(k_j^{m+1}x+\sigma t)} \\ &\quad -\tfrac{1}{\sqrt{2}}\alpha_0\,m^{\frac{1}{2}}\sum_{j=1}^{2}\frac{P_j^{m-1}}{k_j^{m-1}+\omega/c}\int_{L_j}^{x}\mathrm{e}^{-\mathrm{i}k_j^{m-1}x}\,X\,\mathrm{d}x\,\mathrm{e}^{\mathrm{i}(k_j^{m-1}x+\sigma t)} \\ &\quad +\delta_{m0}\frac{\tau_{0n}}{2c}\int_{L_2}^{x}\mathrm{e}^{\mathrm{i}(\omega/c)x}\,X\,\mathrm{d}x\,\mathrm{e}^{\mathrm{i}[-(\omega/c)x+\sigma t)} \end{aligned} \tag{38}$$

where δ_{m0} is the Kronecker δ-function ($\delta_{m0}=1$ when $m=0$; $\delta_{m0}=0$ if $m\neq 0$), and R, S, and T are defined in the obvious manner.

The p_m-field can be found in a manner completely analogous to that for the u_m-field. The two fields have very similar forms; p_m is just u_m multiplied by c and with the sign of R reversed, that is,

$$p_m(x) = c[-\tfrac{1}{\sqrt{2}}(m+1)^{\frac{1}{2}}R+\tfrac{1}{\sqrt{2}}m^{\frac{1}{2}}S+\delta_{m0}\,T]. \tag{39}$$

In summary, the solutions to (11) in an unbounded ocean are

$$q_n = \sum_{m=0}^{M} q_m\,\phi_m(\eta), \tag{40}$$

where q is u, v, or p. Just as in the sum over vertical modes, in principle, an infinite number of Hermite functions contribute to the sum (40). In practice, the upper limit must be truncated at a finite value M, and this approach will be useful only if the series converge rapidly enough with m so that M need not be too large. Again, for realistic choices of ν and $\rho_b(z)$, rapid convergence is assured.

(c) *The presence of radiation*

Let k be any of the quantities k_1^m, k_2^m, or $-\omega/c$. Then each term of (33), (38), and (39) has the form

$$\left\{\text{const.}\int_{\pm\infty}^{x}\mathrm{e}^{-\mathrm{i}kx}\,X\,\mathrm{d}x\right\}\mathrm{e}^{\mathrm{i}(kx+\sigma t)}. \tag{41}$$

This expression clearly describes a wave with wavenumber k, frequency σ, and amplitude given by the expression in curly brackets.

In the absence of friction in the deep ocean, so that $\omega=\sigma$, these waves are the familiar undamped equatorially trapped Rossby and Kelvin waves. The wavenumbers k_1^m, k_2^m, and $-\omega/c$

correspond to Rossby waves, with westward and eastward group velocities, and the Kelvin wave, respectively. In the presence of friction, ω is complex, and the wavenumbers necessarily have an imaginary part. However, it is still possible to interpret the waves as Rossby and Kelvin waves. They have the same meridional structure as the inviscid waves, and differ only in that now they are damped in the direction of their group velocity. It is useful to keep the analogy with the inviscid waves even when $\sigma \to 0$. In this limit, where $\omega = -\mathrm{i}\,A/c^2$, all wavenumbers are purely imaginary. Rossby and Kelvin waves no longer propagate away from their source region, but simply decay from it.

Note that the amplitude in (41) is proportional to an integral of X, rather than X itself. Therefore, the amplitude is not necessarily zero outside the wind-forced region. The choice of lower limit in these integrals thus governs whether radiation appears to the east, the west, or on both sides of the wind patch. Waves with eastward (westward) group velocity can appear only east (west) of the patch. Equivalently, in the steady state, waves that decay eastward (westward) can appear only east (west) of the patch. The choice (34) satisfies these requirements.

(*d*) *Boundary effects*

The unbounded response (40) does not satisfy the constraint (20). It is necessary to add to it packets of free waves excited at the ocean boundaries (Moore & Philander 1978; Cane & Sarachik 1977; McCreary 1976, 1977). Waves generated at western boundaries, designated by a prime, must have eastward group velocities. Rossby waves with eastward group velocity are

$$\left.\begin{aligned} u'_m &= A_m\left[\phi_{m+1} - \frac{ck_2^m+\omega}{ck_2^m-\omega}\left(\frac{m}{m+1}\right)^{\frac{1}{2}}\phi_{m-1}\right]\mathrm{e}^{\mathrm{i}k_2^m(x-x_0)},\\ v'_m &= \frac{\mathrm{i}}{c\alpha_0}\,\frac{ck_2^m+\omega}{\frac{1}{\sqrt{2}}(m+1)^{\frac{1}{2}}}\,A_m\,\phi_m\,\mathrm{e}^{\mathrm{i}k_2^m(x-x_0)},\\ p'_m &= cA_m\left[\phi_{m+1} + \frac{ck_2^m+\omega}{ck_2^m-\omega}\left(\frac{m}{m+1}\right)^{\frac{1}{2}}\phi_{m-1}\right]\mathrm{e}^{\mathrm{i}k_2^m(x-x_0)}, \end{aligned}\right\} \tag{42}$$

where $m = 0, 1, 2, \ldots$, and A_m is an arbitrary amplitude. The $m = 0$ wave is the Yanai wave. An additional eastward propagating wave, labelled the $m = -1$ wave, is the equatorially trapped Kelvin wave,

$$u'_{-1} = A_{-1}\,\phi_0\,\mathrm{e}^{-\mathrm{i}(\omega/c)(x-x_0)}, \quad p'_{-1} = cu'_{-1}, \quad v'_{-1} = 0. \tag{43}$$

Waves generated at eastern boundaries, designated by a double prime, must have westward group velocities. The appropriate Rossby waves are

$$\left.\begin{aligned} u''_m &= B_m\left[\frac{ck_1^m-\omega}{ck_1^m+\omega}\left(\frac{m+1}{m}\right)^{\frac{1}{2}}\phi_{m+1} - \phi_{m-1}\right]\mathrm{e}^{\mathrm{i}k_1^m(x-x_1)},\\ v''_m &= \frac{\mathrm{i}}{c\alpha_0}\,\frac{ck_1^m-\omega}{\frac{1}{\sqrt{2}}m^{\frac{1}{2}}}\,B_m\,\phi_m\,\mathrm{e}^{\mathrm{i}k_1^m(x-x_1)},\\ p''_m &= cB_m\left[\frac{ck_1^m-\omega}{ck_1^m+\omega}\left(\frac{m+1}{m}\right)^{\frac{1}{2}}\phi_{m+1} + \phi_{m-1}\right]\mathrm{e}^{\mathrm{i}k_1^m(x-x_1)}, \end{aligned}\right\} \tag{44}$$

where $m = 1, 2, 3, \ldots$, and B_m is an arbitrary amplitude. The set begins at $m = 1$ because there are no westward propagating equivalents of the Yanai and Kelvin waves.

At a western ocean boundary each A_m is chosen to cancel all components of zonal flow proportional to ϕ_{m+1}. One component arises from (38), $u_{m+1}(x_0)$. The Rossby waves u''_m and u''_{m+2}

contribute two other pieces. The u'_{m+2} Rossby wave leaving the western boundary makes a final contribution. With the aid of (42) and (44) it follows that each A_m is given by

$$A_m = \left(\frac{m+2}{m+3}\right)^{\frac{1}{2}} \frac{ck_2^{m+2}+\omega}{ck_2^{m+2}-\omega} A_{m+2} - \left(\frac{m+1}{m}\right)^{\frac{1}{2}} \frac{ck_1^m-\omega}{ck_1^m+\omega} e^{-ik_1^m d} B_m + e^{-ik_1^{m+2}d} B_{m+2} - u_{m+1}(x_0), \quad (45)$$

where $m = -1, 0, 1, \ldots, M$. At an eastern ocean boundary each B_m is picked to cancel all components of zonal flow proportional to ϕ_{m-1}. By similar arguments

$$B_m = \left(\frac{m-1}{m-2}\right)^{\frac{1}{2}} \frac{ck_1^{m-2}-\omega}{ck_1^{m-2}+\omega} B_{m-2} - \left(\frac{m}{m+1}\right)^{\frac{1}{2}} \frac{ck_2^m+\omega}{ck_2^m-\omega} e^{ik_2^m d} A_m + e^{ik_2^{m-2}d} A_{m-2} + u_{m-1}(x_1), \quad (46)$$

where $m = 1, 2, 3, \ldots, M$. In both (45) and (46), $B_0 = B_{-1} = 0$.

In principle, the number of boundary waves needed is infinite. In practice, only a finite number, M, of waves are used. Another radiation condition requires that $A_{M+2} = A_{M+1} = 0$. This choice ensures that there are no sources of energy at high latitudes along the western boundary. In that case, (45) and (46) form a system of $2M+2$ equations in the $2M+2$ unknowns, $A_{-1}, \ldots, A_M, B_1, \ldots, B_M$. They can be written down in the form of a highly banded matrix equation, which can be solved economically on a computer. In summary, the solutions to (11) that satisfy (20) are

$$q_n = \sum_{m=0}^{M} q_m \phi_m(\eta) + \sum_{m=-1}^{M} q'_m + \sum_{m=1}^{M} q''_m, \quad (47)$$

where q is u, v, or p.

It is possible to alter the approach outlined above to find the boundary response generated in an ocean with a single ocean boundary. If the model has only an eastern boundary, set $A_m = 0$ for all m, and use (46) to find B_m. If the model has only a western ocean boundary, set $B_m = 0$ for all m, and use (45) to find A_m.

4. Results

The model was used to study the response of the ocean to a wind field representative of the steady trades in the Pacific Ocean. The wind has the form (18) with $\tau_0 = -0.5\,\mathrm{dyn/cm^2}$, $\sigma = 0$,

$$X(x) = \begin{cases} \cos(\pi x/\Delta x), & |x| \leqslant \frac{1}{2}\Delta x, \\ 0, & |x| > \frac{1}{2}\Delta x, \end{cases} \quad (48)$$

and

$$Y(y) = (1 + y^2/\Delta y^2)\, e^{-y^2/\Delta y^2}, \quad (49)$$

where $\Delta x = 5000$ km and $\Delta y = 1000$ km. For $y < \Delta y$, $Y(y)$ is virtually constant, and so there is only a weak wind curl in the tropical ocean. Along the equator wind curl vanishes. The shaded region of figure 3 indicates the extent of the wind patch, and the thin line its zonal profile, (48).

Figure 2 shows seven different profiles of background density structure $\rho_b(z)$. Profile 1 varies linearly with depth beneath a surface mixed layer of thickness $H = 75$ m. The remaining curves are described by

$$\rho_b(z) = \begin{cases} \rho_0, & z > -H, \\ \rho_0 + \Delta\rho_1[1 - e^{-(z+H)/b_1}] + \Delta\rho_2[1 - e^{-(z+H)/b_2}], & z \leqslant -H, \end{cases} \quad (50)$$

where $b_1 = 200$ m, $b_2 = 1000$ m. For profile 2, $\Delta\rho_1 = 0$, $\Delta\rho_2 = 0.005$, and $H = 75$ m. The unlabelled curves have a strong near-surface pycnocline where $\Delta\rho_1 = 0.003$, $\Delta\rho_2 = 0.002$. They differ only in that $H = 0$, 50, 75, 100, and 150 m. Unless stated otherwise, $\rho_b(z)$ is always given by the thicker curve. This profile is typical of the density structure in the central tropical Pacific (Reid 1965).

PHILOSOPHICAL TRANSACTIONS OF THE ROYAL SOCIETY A MATHEMATICAL, PHYSICAL & ENGINEERING SCIENCES

The size of the mixing coefficients, $\nu = \kappa = A/N_b^2$, varies considerably with depth. If there is a surface mixed layer, they are infinitely large there. Just beneath the mixed layer N_b attains its maximum value, and so ν and κ reach a minimum, ν_{min}. At greater depths N_b decreases (except for profile 1 of figure 2) and they can attain a much larger value. ν_{min} is a measure of the amplitude of mixing in the immediate vicinity of the Undercurrent. Unless stated otherwise, A is always chosen so that $\nu_{min} = 0.55$ cm^2/sec. This choice is consistent with minimum values of eddy viscosity measured at the core of the Atlantic Equatorial Undercurrent (Crawford 1976). When $\rho_b(z)$ is the thicker curve of figure 2 and $\nu_{min} = 0.55$ cm^2/s, the value of ν at the ocean bottom is 57 cm^2/s.

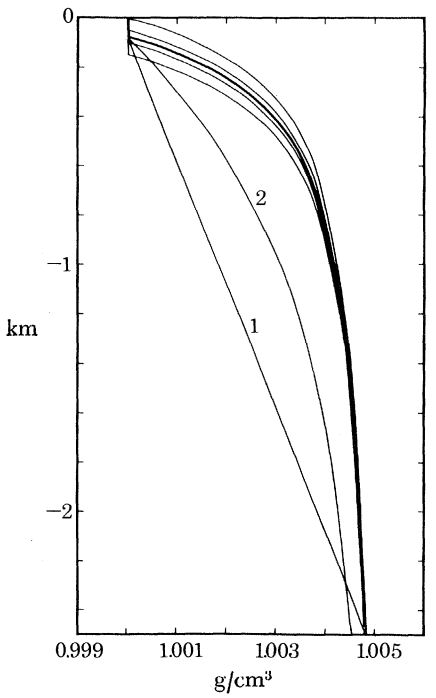

FIGURE 2. Profiles of background density structure, $\rho_b(z)$. Profile 1 has a constant gradient below the mixed layer. The remaining profiles are described by equation (50). The unlabelled curves have a strong near-surface pycnocline typical of the tropical Pacific, and differ only in the thickness of the surface mixed layer. Most results correspond to the thicker curve.

Unless stated otherwise, the model ocean has both eastern and western boundaries, at $x_0 = -5000$ km and $x_1 = 5000$ km. The positions of the boundaries are indicated in figure 3. The depth of the ocean is $D = 2500$ m.

It is necessary to choose sufficiently large values of N and M in the sums (10) and (47). In a series of tests N and M were varied over a wide range of values and solutions were compared. For $N \geqslant 50$, $M \geqslant 35$ they were virtually identical. The results discussed here have $N = 100$, $M = 70$ and so are more than adequately resolved.

(*a*) *The model Undercurrent*

Six velocity sections describe the three-dimensional flow field. Figure 3 shows the positions of these sections relative to the equator and ocean boundaries. Figures 4*a–f* show the zonal and meridional circulation patterns of sections 1–5, respectively.

The zonal flow has features that compare very well with observation. There is an eastward

equatorial jet situated in the main thermocline just beneath the mixed layer. The e-folding width scale of this jet is less than 200 km, and it is about 100 m thick. Its speed increases steadily away from both boundaries and reaches a maximum of about 150 cm/s slightly to the east of the wind stress maximum. A surface westward flow reaches a maximum somewhat greater than 70 cm/s. Westward flow also exists beneath the Undercurrent. This flow extends to about 400 m and reaches a maximum speed greater than 20 cm/s. Slightly off the equator all strong zonal currents are in geostrophic balance. Even at the equator they are consistent with geostrophy in that the meridional curvature of the pressure field, p_{yy}, is given by $-\beta u$.

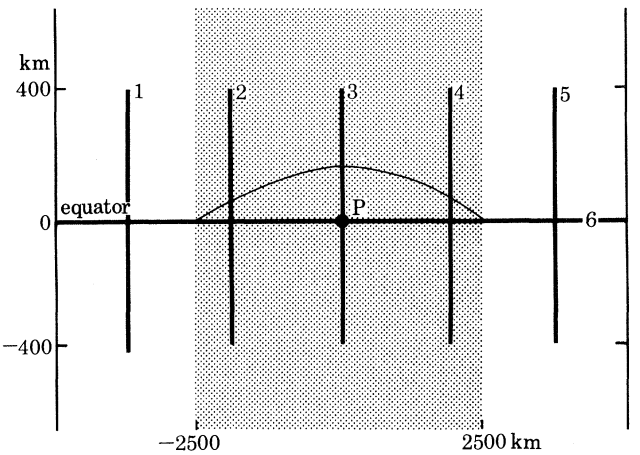

FIGURE 3. A schematic diagram showing the location of sections 1–6, the position of ocean boundaries, and the structure of the wind field. The shaded region indicates the extent of the wind field, and the thin line its zonal profile. Its meridional profile is very nearly latitude-independent. Wind stress is entirely westward and reaches a maximum of 0.5 dyn/cm² in the centre of the ocean basin. The structure of the wind is described more precisely in equations (48) and (49).

The meridional circulation patterns are also familiar. Along section 3, at the wind maximum, there is a strong divergence of surface water from the equator; upwelling occurs above the core of the Undercurrent at speeds as great as 0.0025 cm/s, and weaker downwelling occurs beneath the core. There is a convergence of water at and slightly above the core at speeds approaching 10 cm/s. Along sections 2 and 4, where the driving wind is weak, the meridional circulation is also weak but otherwise similar to that of section 3. Maximum upwelling, represented by the fifth line of arrows in figure 4f, occurs at the point of the greatest zonal flow. The sign and amplitude of u_x determine the strength of convergence or divergence of fluid from the current core. The meridional circulation patterns of sections 1 and 5, where there is no wind, are driven entirely by this effect. Maximum divergence (convergence) of fluid occurs near the eastern (western) edge of the wind patch.

In the western ocean equatorial pressure is higher everywhere by 9 dyn cm, and in the eastern ocean it is lower everywhere by 6 dyn cm. In the central ocean the surface eastward pressure gradient force reaches a maximum of 5×10^{-5} dyn/g (equivalent to a sea level inclination of -5×10^{-8}). At the depth of the current core the pressure force reduces to half its surface value, and at greater depths it becomes weakly negative. This equatorial pressure field is consistent with the observations of Knauss (1966) as well as the calculations of Arthur (1960).

The density field, that is, $\rho_b(z) + \rho(x, y, z)$, has expected features. For example, along section 3 isopycnals at depths shallower than the core of the Undercurrent bend sharply upward within

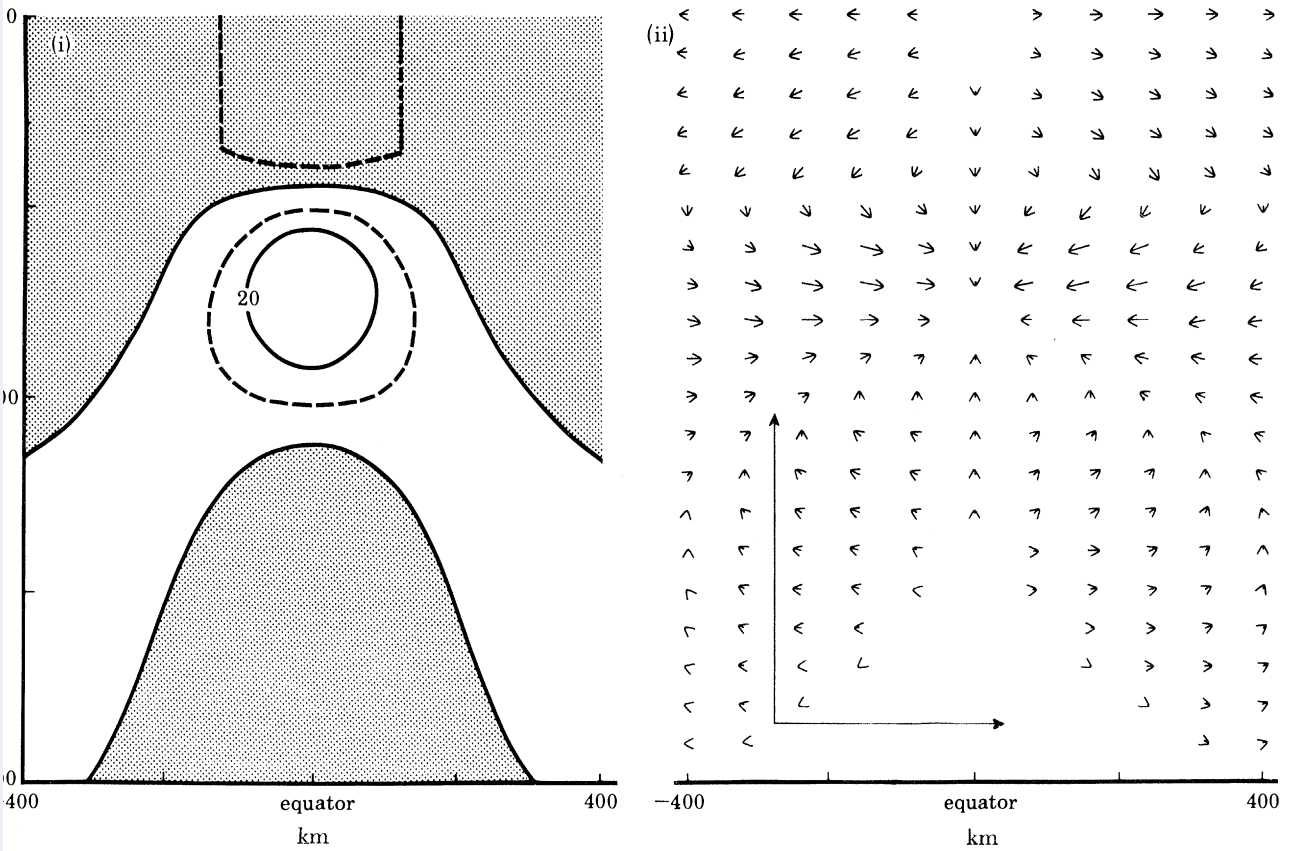

FIGURE 4*a*. Vertical sections of (i) zonal velocity and (ii) meridional circulation along section 1 of figure 3. The contour interval is 20 cm/s; the dashed contours are ± 10 cm/s. Calibration vectors in the lower left corner of (ii) have amplitudes 0.005 cm/s and 10 cm/s in the vertical and horizontal directions, respectively.

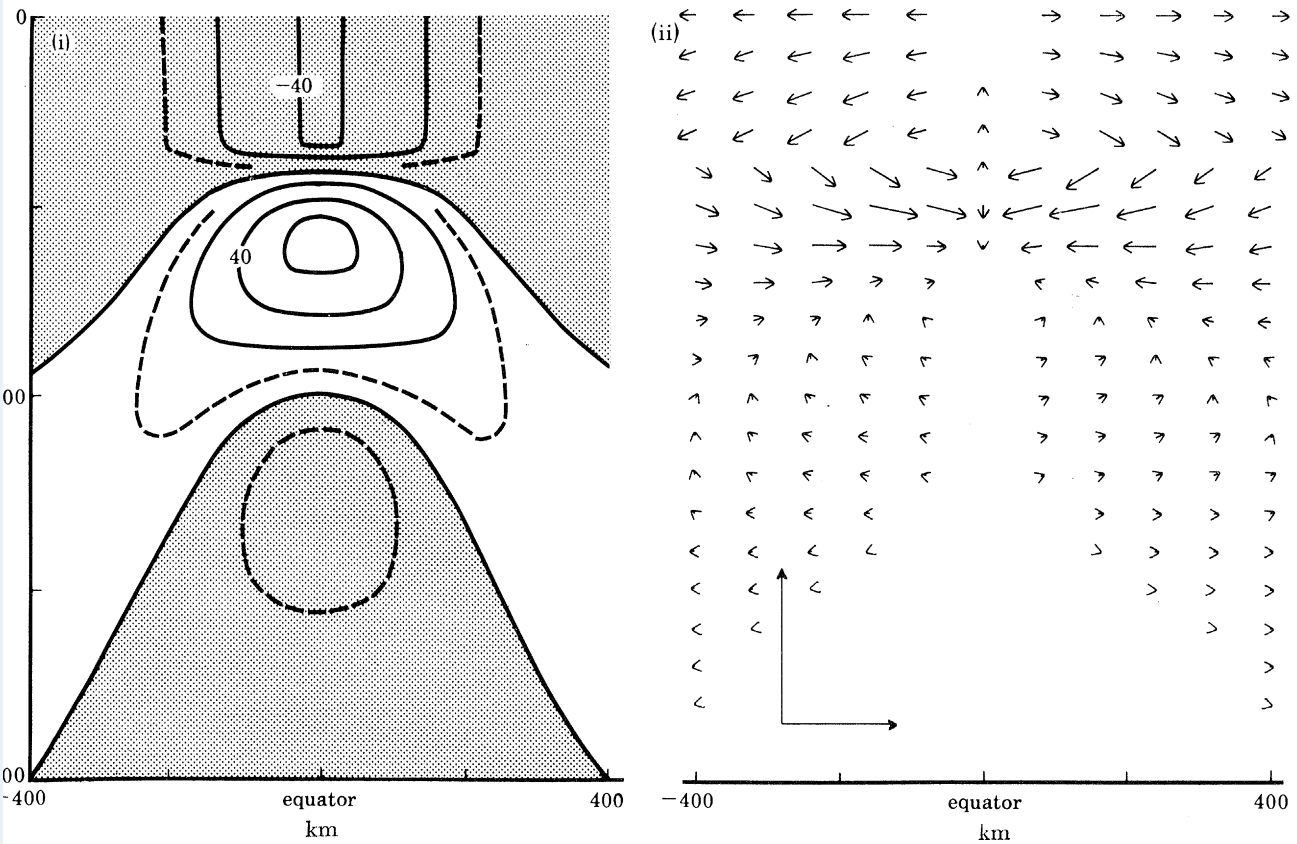

FIGURE 4*b*. Same as for figure 4*a*, but along section 2 of figure 3.

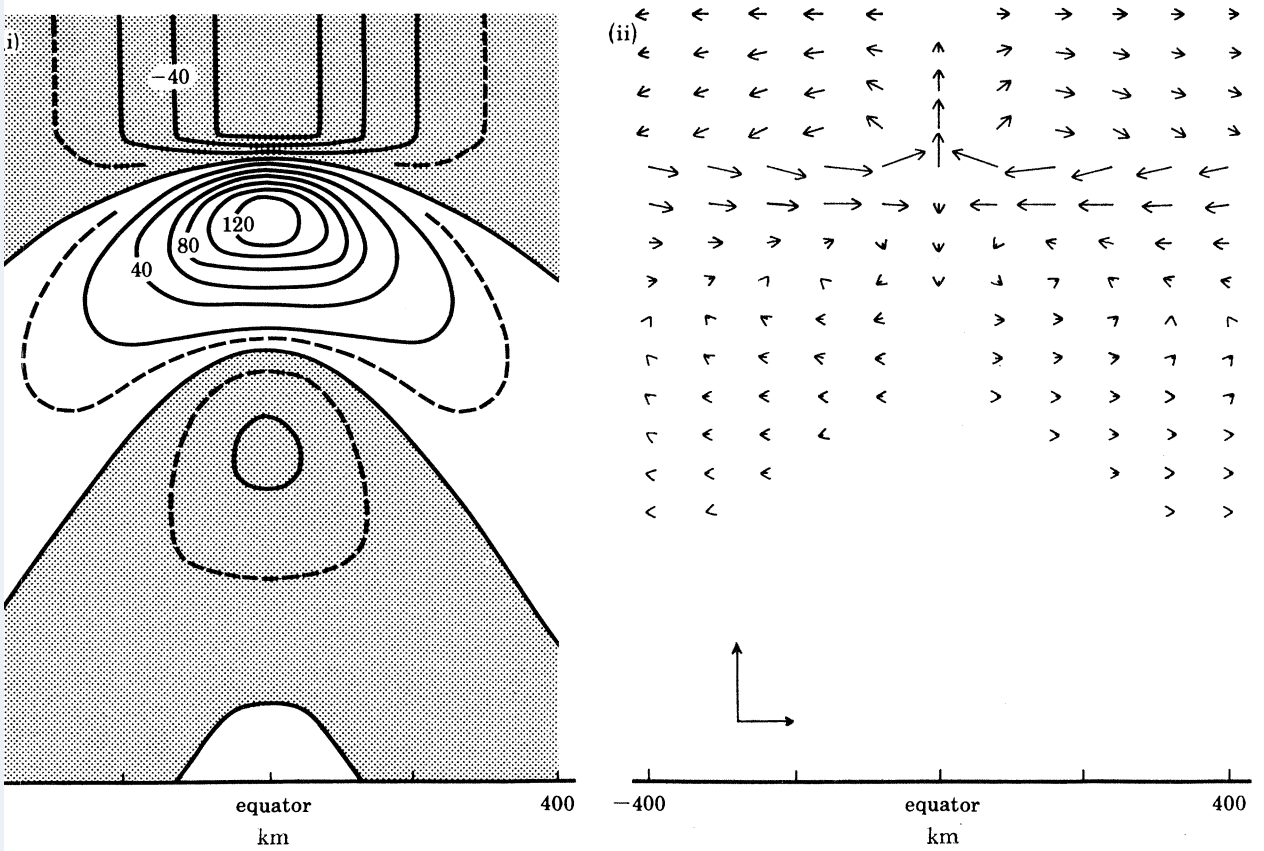

FIGURE 4*c*. As for figure 4*a*, but along section 3 of figure 3.

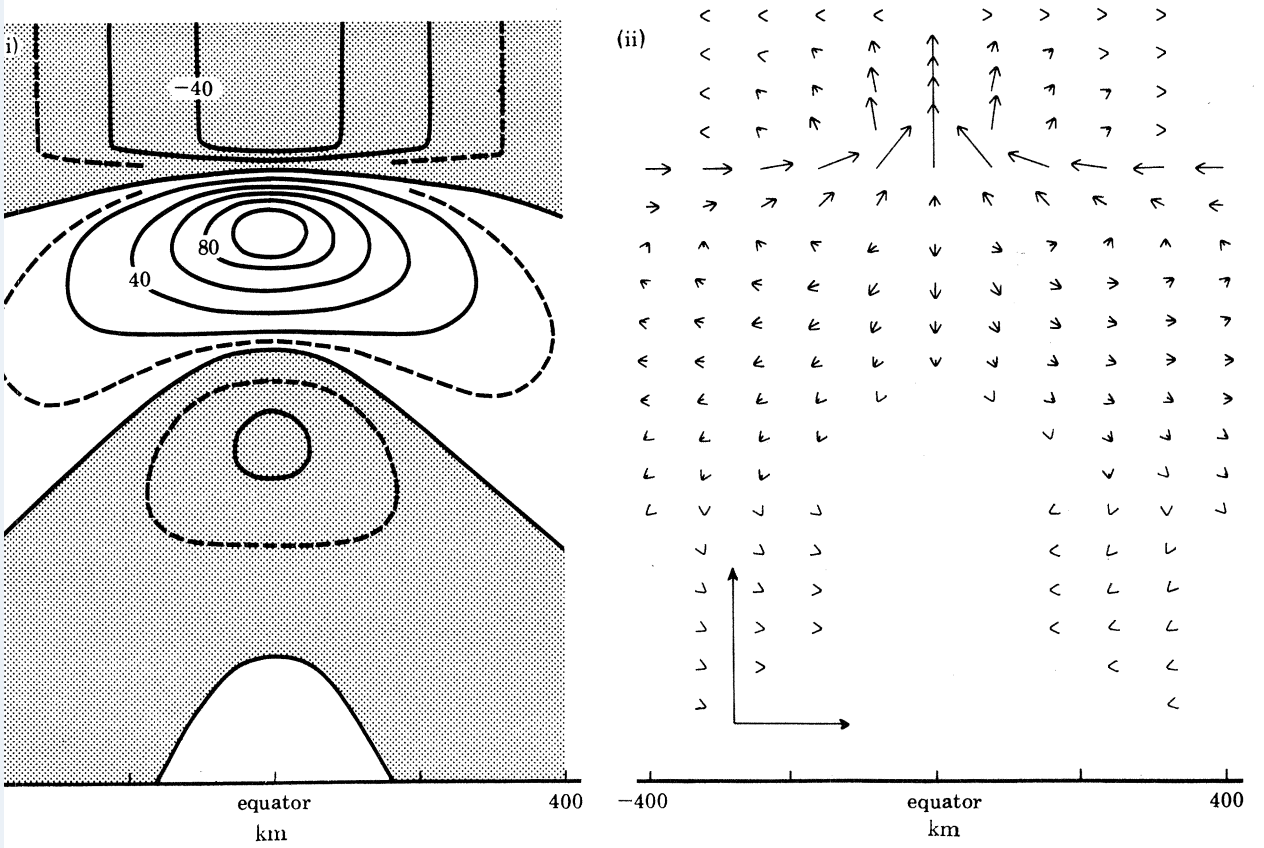

FIGURE 4*d*. As for figure 4*a*, but along section 4 of figure 3.

200 km of the equator to intersect the bottom of the mixed layer. Isopycnals at depths somewhat greater than that of the current core bend downward. At greater depths isopycnals again bend upward (but weakly), indicating the presence of the Equatorial Intermediate Current.

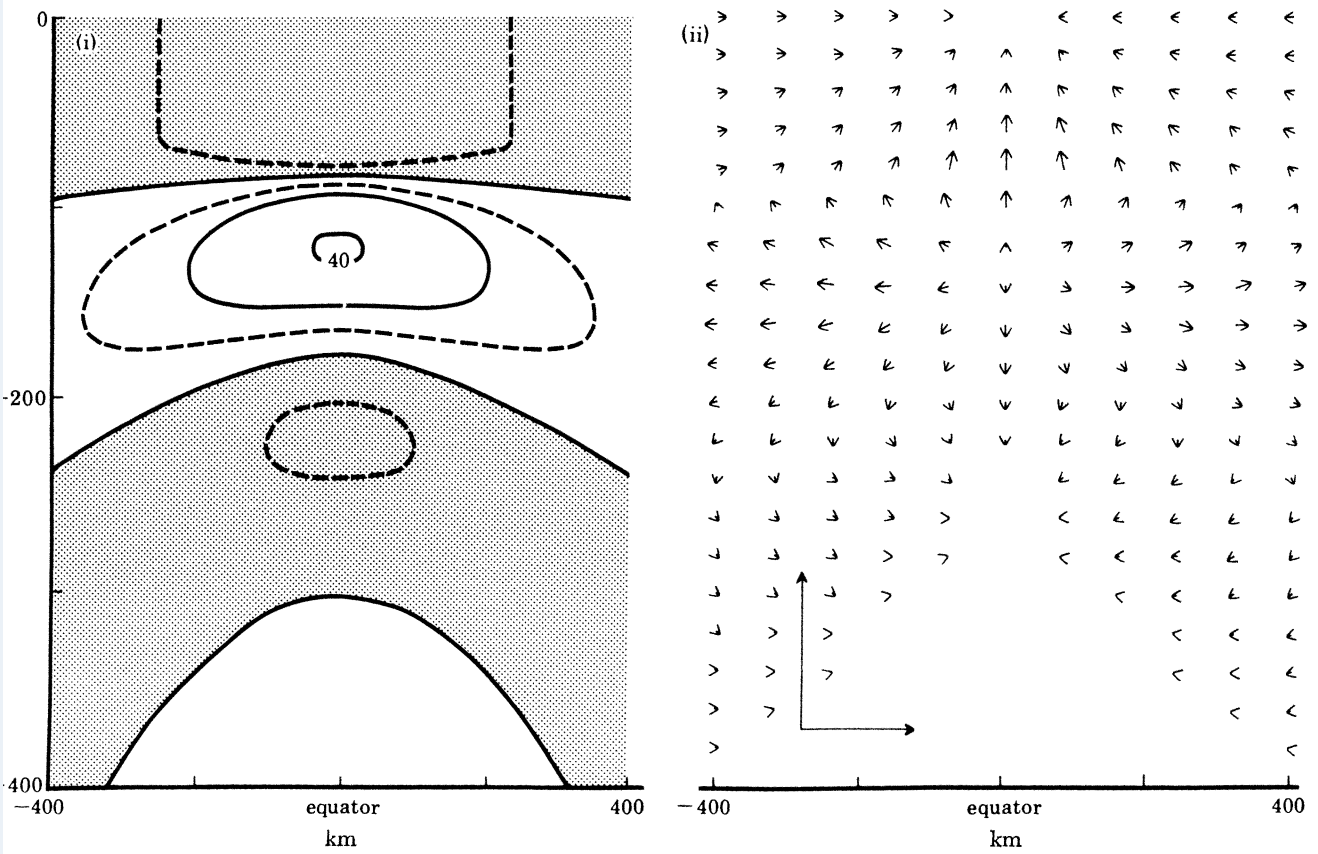

FIGURE 4*e*. As for figure 4*a*, but along section 5 of figure 3.

However, the density field also has unrealistic aspects which point out the limitations of the linearization of the equation of heat conservation. As discussed above, a density inversion necessarily exists at the base of the mixed layer wherever there is downwelling. Downwelling occurs in the model off the equator in the central ocean and everywhere in the western ocean. The amplitude of this inversion reaches a maximum of almost 0.0015 g/cm^3 slightly off the equator near the western edge of the wind patch. In the central and eastern ocean, where the divergence of fluid from the core of the Undercurrent is strongest and the equatorial spreading of isopycnals is most intense, another region of static instability exists at and below the current core. Its width and vertical extent increase markedly toward the east, reaching values of ± 480 km and 100 m. The maximum density inversion is 0.002 g/cm^3 over a depth of 100 m and occurs at the equator near the eastern edge of the wind patch. It is interesting that these two regions of static instability coincide with the two regions in the Pacific Ocean where mixing apparently plays a surprisingly strong role: the thick surface mixed layer in the western Pacific, and the thermostad in the eastern Pacific (Tsuchiya 1975; Philander 1973, figure 7).

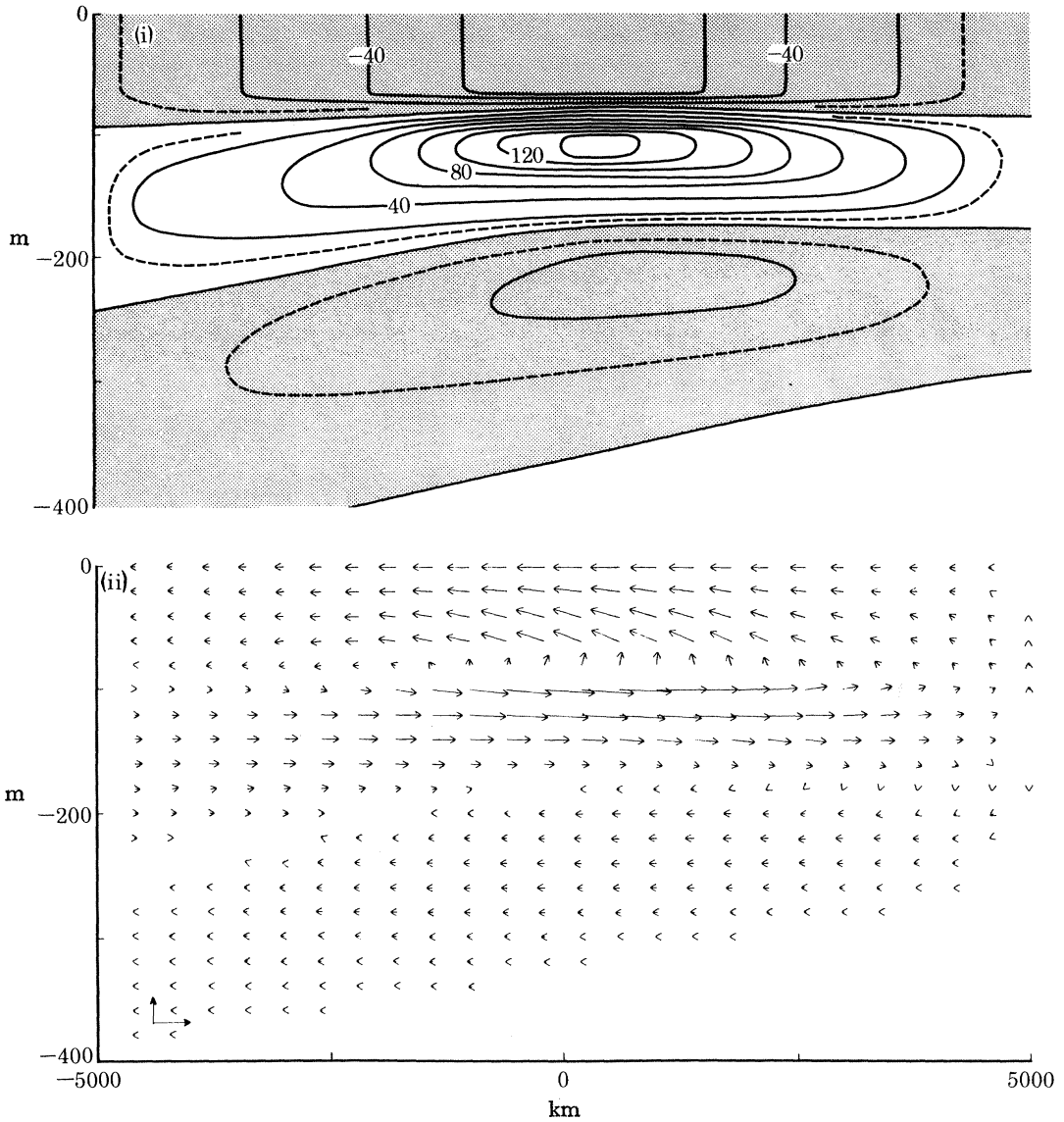

FIGURE 4*f*. Velocity sections along section 6 of figure 3. (i) Contours of zonal velocity. The contour interval is 20 cm/sec with dashed contours, ± 10 cm/s. (ii) Vector plot of both the zonal and vertical velocity fields. Calibration vectors in the lower left corner have amplitudes 0.005 cm/s and 100 cm/s in the vertical and horizontal directions, respectively.

(*b*) *The dependence on model parameters*

It is important to know how the response of the model depends on the free parameters $\rho_b(z)$ and ν. Do solutions vary strongly as ν_{min}, the amplitude of mixing at the core of the Undercurrent, changes? Does the response depend critically on the vertical structure of ν? Is the presence of a strong surface pycnocline or the existence of a mixed layer necessary for the generation of a realistic Undercurrent? To answer these questions figures 5–7 compare profiles of zonal velocity over a wide range of parameter values. All profiles are taken at the centre of the ocean basin, point P of figure 3. In each figure the thicker reference curve is just that of the model Undercurrent discussed above.

PHILOSOPHICAL TRANSACTIONS OF THE ROYAL SOCIETY A MATHEMATICAL, PHYSICAL & ENGINEERING SCIENCES

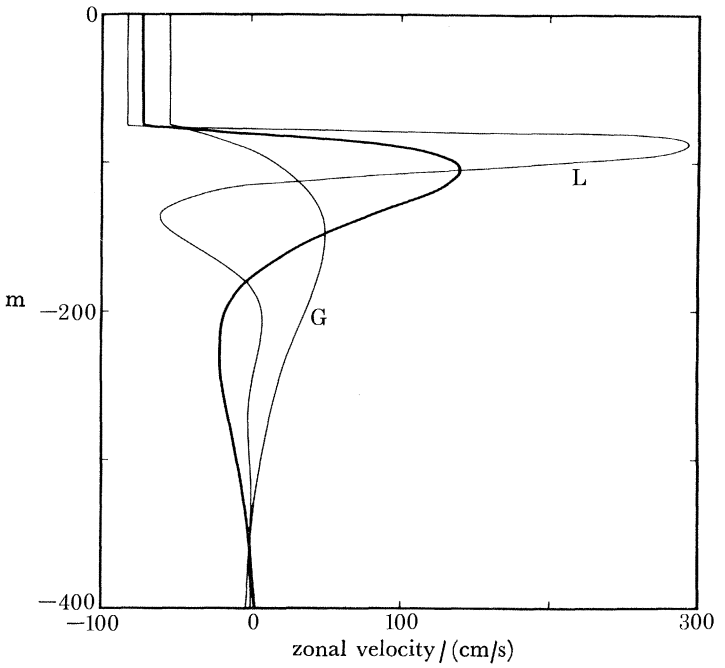

FIGURE 5. Profiles of zonal velocity at point P of figure 3, contrasting the model response for three different values of ν_{min}. Curves G and L correspond to $\nu_{min} = 5.3$ and 0.069 cm²/s, respectively. The thicker curve corresponds to $\nu_{min} = 0.55$ cm²/s. The maximum speed of the Undercurrent varies more weakly than $\nu_{min}^{-\frac{1}{2}}$.

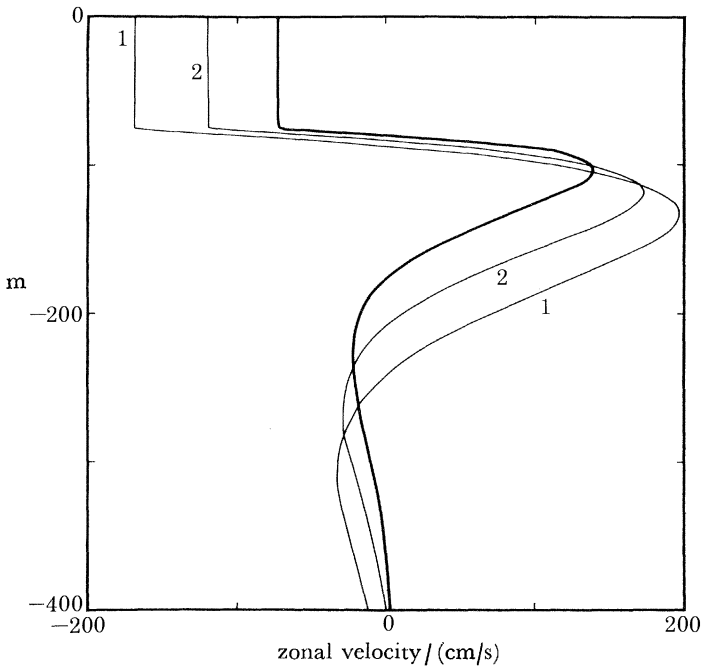

FIGURE 6. Profiles of zonal velocity at point P of figure 3, contrasting the model response for three different background density structures. Profiles 1 and 2 correspond to curves 1 and 2 of figure 2, respectively. The thicker profile corresponds to the thicker curve of figure 2. The profiles are very insensitive to the shape of $\rho_b(z)$ beneath the mixed layer.

PHILOSOPHICAL TRANSACTIONS OF THE ROYAL SOCIETY A MATHEMATICAL, PHYSICAL & ENGINEERING SCIENCES

Figure 5 compares solutions in which $\nu_{\min}$ varies but $\rho_b(z)$ remains fixed. In this way the amplitude of ν changes, but not its structure with depth. Profiles G and L show the model's response when $\nu_{\min} = 5.3$ and 0.069 cm^2/s, respectively. As $\nu_{\min}$ weakens, the Undercurrent becomes stronger, shallower, and thinner, but the basic pattern of the equatorial currents remains the same. While $\nu_{\min}$ decreases by a factor of 75, the maximum speed of the Undercurrent increases only by a factor of 6, the depth of the current core shallows by a factor of 2, and the jet thins by a factor of 6. The e-folding width of the jet decreases by a factor of 2. So, although the results of the model depend on the choice of $\nu_{\min}$, the dependence is weak. This property is surprising, since in homogeneous layer models the flow field depends strongly on the strength of vertical mixing. For example, in Stommel's model the maximum speed of the Undercurrent is inversely proportional to the mixing parameter, whereas here its speed varies more weakly than $\nu_{\min}^{-\frac{1}{2}}$.

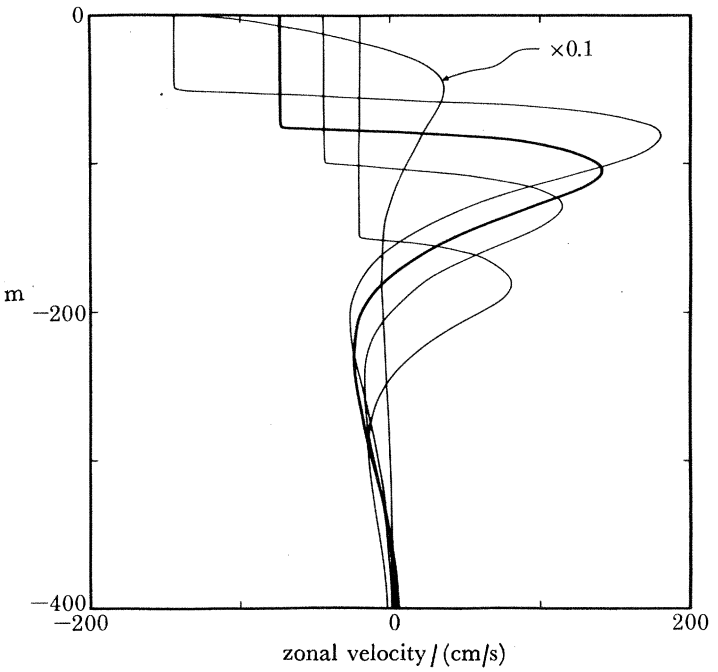

FIGURE 7. Profiles of zonal velocity at point P of figure 3, contrasting the model response for five different values of mixed layer depth, H. The profiles correspond to the five unlabelled curves of figure 2. For convenience of display, the profile with $H = 0$ is decreased in amplitude by a factor of 10, so that the surface velocity field is actually -1410 cm/s and the maximum speed of the Undercurrent is somewhat greater than 300 cm/s. The surface mixed layer is necessary to obtain realistic surface velocities, but other aspects of the flow depend weakly on H.

Figure 6 compares solutions in which the deep density structure of the ocean varies, but $\nu_{\min}$ remains fixed at 0.55 cm^2/s. In this way the vertical structure of ν changes, but its amplitude in the vicinity of the Undercurrent remains relatively unchanged. Profiles 1 and 2 show the model response for the density structures 1 and 2 of figure 2, respectively. As the pycnocline becomes increasingly confined to the surface, the Undercurrent becomes slightly weaker, shallower, and thinner. There is no indication that its width changes. Evidently the model is very insensitive to changes in the deeper density structure of the ocean. It also follows that the model is quite independent of values of eddy viscosity in the deep ocean, even though they can be very large there.

Figure 7 compares solutions in which only the depth of the mixed layer is changed; the shape of the deep pycnocline is unaltered, and the value of $\nu_{\min}$ again remains fixed at 0.55 cm^2/s. The profiles show the model response for the unlabelled density structures of figure 2. As H decreases, the Undercurrent becomes somewhat stronger and shallower, but its thickness remains the same. Again, there are no appreciable changes in the width of the jet. Much more significant changes occur in the surface drift. As H decreases from 150 to 50 m, the surface drift increases markedly by a factor of 7. When H vanishes, the flow reaches the absurdly large value of -1410 cm/s. Clearly, the presence of a sufficiently thick ($H \gtrsim 50$–75 m) turbulent surface layer is necessary in this model to obtain realistic surface velocities.

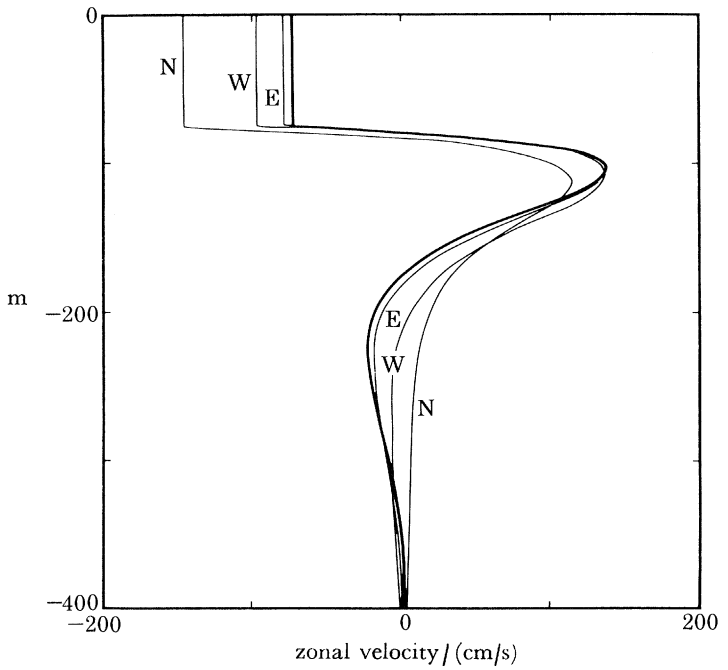

FIGURE 8. Profiles of zonal velocity at point P of figure 3 with and without ocean boundaries. The curves labelled N, E, and W correspond to ocean basins with no boundaries, a single eastern boundary, and a single western boundary, respectively. The thicker curve corresponds to an ocean basin with both boundaries. Only profile N lacks westward flow at depth.

(*c*) *The effect of ocean boundaries*

How important are ocean boundaries for the generation of the model Undercurrent? Figure 8 compares solutions from both bounded and unbounded ocean basins. For profile E (W) the ocean has a single eastern (western) boundary. The thicker reference curve is that of the model Undercurrent and has both boundaries. Profile N shows the model response when the ocean has neither boundary. The similarity of these curves shows that ocean boundaries are not necessary for maintaining the Undercurrent. (It is only necessary that the wind stress is bounded.) However, the differences among the curves suggest that boundary effects do extend well back into the ocean interior. The presence of boundaries considerably weakens the surface flow and intensifies the Undercurrent. Significantly, the unbounded response has no westward current beneath the Undercurrent. Therefore, the presence of the Equatorial Intermediate Current is due entirely to effects radiated from boundaries.

5. Dynamics

One way of describing the dynamics of ocean models is simply to state the dominant balances of terms in the equations of motion. (Complicated numerical models are to a large extent limited to this approach.) For the present model this list of balances is very short, and not very revealing, because the equations themselves are so simple. Off the equator the momentum equations are very nearly in Ekman balance. As a result, for easterly winds there is a divergence of surface waters from the equator and subsequent upwelling there, just as in the Stommel model. At the equator baroclinic pressure gradients are important in the momentum equations. Strong zonal jets are in geostrophic balance there, and the zonal pressure gradient force balances the downward diffusion of momentum as in the Arthur calculation. There are no clues from this list of balances that suggest how the baroclinic pressure field is generated, nor is there any indication why the flow field is so narrow and remains so strongly trapped near the ocean surface. Finally, the role of radiation in the dynamics is not explained.

The method of solution adopted here, that is, the expansion into vertical normal modes, allows another and more enlightening way of discussing the dynamics. Rather than describing the dominant balances that govern the total flow field, it is possible instead to describe those balances that occur for individual modes. In this way the three-dimensional dynamics of equations (1) can be understood by using concepts appropriate to the simpler two-dimensional dynamics of equations (11).

A nomenclature does not yet exist that labels various balances of (11). So, in the first part of this section simpler models that illustrate important balances are discussed and labelled. Because the flow fields generated by these simpler models have very unrealistic features, they also demonstrate the necessity of both stratification and diffusion in the equatorial ocean. In the remainder of the section this nomenclature is used to show how the presence of radiation affects the equatorial currents.

(*a*) *The necessity of stratification and diffusion*

A model that illustrates the importance of stratification in the equatorial ocean ignores the baroclinic (but not the barotropic) pressure gradients in (11). This dynamics is essentially that studied by Stommel (1960); the only difference is that here the eddy viscosity is not necessarily constant. The steady-state solution for each vertical mode is

$$\left.\begin{aligned} v_n &= -\tau_{0n}\frac{\alpha_0}{c}X\frac{\eta Y}{\alpha_0^2\eta^2+A^2/c^6},\\ u_n &= (c^2/A)\,(c\alpha_0\eta v_n+F),\\ p_n &= -(c^4/A)\,(\alpha_0 v_{n\eta}+u_{nx}). \end{aligned}\right\} \tag{51}$$

Note that all fields are proportional to X, rather than integrals of X. Therefore, this dynamics is purely local, and the radiation of equatorially trapped waves plays no role. It is useful to refer to a single baroclinic mode, described by (51), as being in Ekman balance, and an oceanic flow in which all baroclinic modes have this form as a baroclinic Ekman flow.

Figure 9 shows a meridional section of baroclinic Ekman flow comparable to that in figure 4*c*; the driving winds and model parameters are the same, and both sections are along section 3. The meridional circulation pattern of figure 9 does serve to illustrate the equatorial pumping process, but otherwise the flow has none of the realistic aspects of figure 4*c*. All velocity components are

absurdly large, the width of the equatorial current system is only about 100 m, and the flow field is not confined to the upper ocean but extends all the way to the ocean bottom. Obviously the presence of baroclinic pressure gradients in the momentum equations is crucial for the generation of a realistic equatorial current structure.

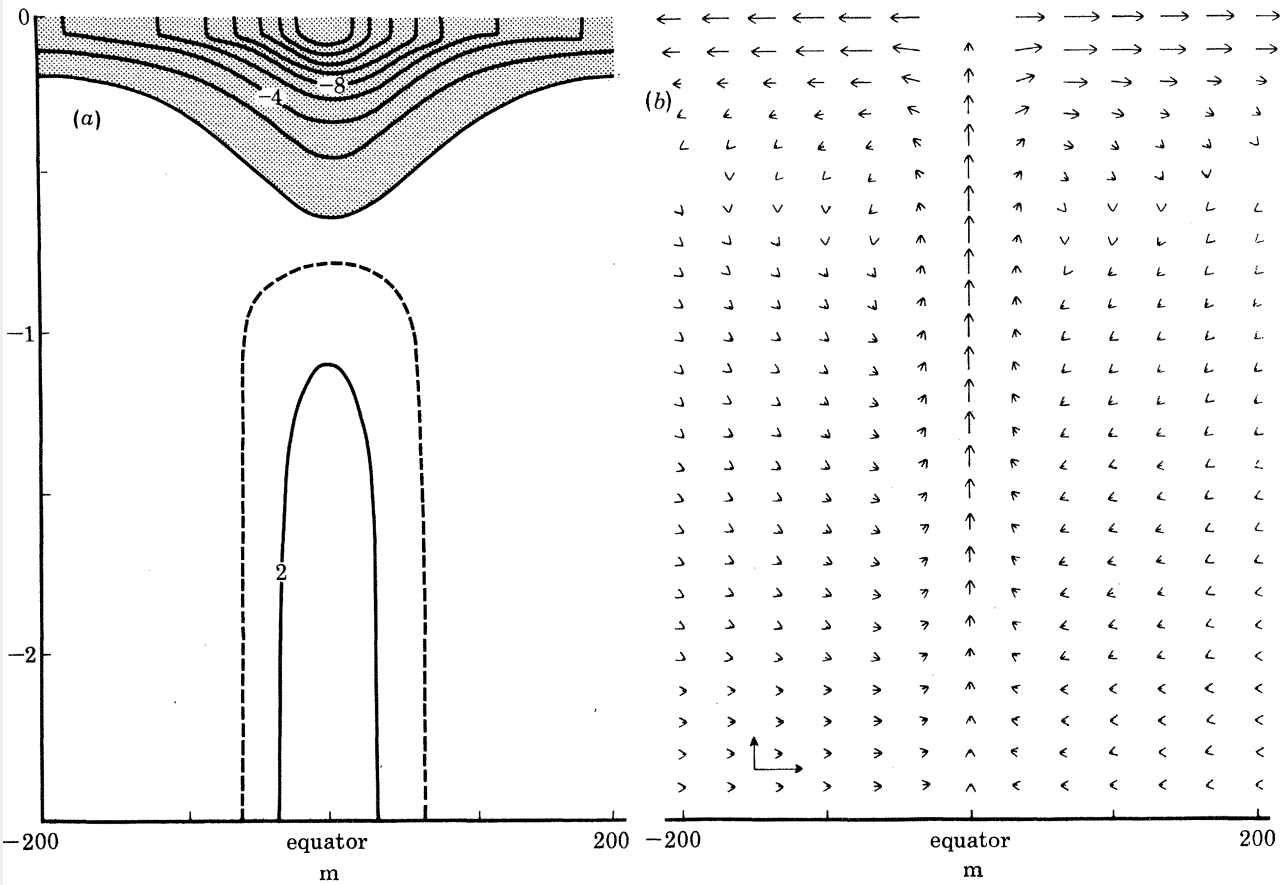

FIGURE 9. Vertical sections of baroclinic Ekman flow, described by equation (51), showing (*a*) zonal velocity and (*b*) meridional circulation along section 3 of figure 3. The contour interval is 1 km/s. Calibration vectors in the lower left corner of the right panel have amplitudes of 100 km/s and 10 km/s in the vertical and horizontal directions, respectively. Horizontal distance is in metres, not kilometres. This flow field, by its absurdity, demonstrates the importance of stratification in the equatorial ocean.

Fundamental limitations of the equatorial Ekman model are evident in (51). A measure of the width of the equatorial current system, L, is the position where v_n reaches a maximum, so that $L = \eta/\alpha_0 = A/\beta c^2$. At this position $v_n = \frac{1}{2}(c^2/A)\,F$. At the equator $w_n = \beta(c^4/A^2)\,F$, and $u_n = (c^2/A)\,F$. All these quantities are so strongly dependent on friction that a realistic Undercurrent cannot be produced, regardless of the value of A (Stommel 1960). Note also that the amplitude of the currents of a given mode varies like c^2F or c^4F, which decrease rapidly with n. Consequently, the lowest-order modes are strongly favoured near the equator. The vertical structure of the solution must look very much like the first baroclinic mode, and there is no evidence of surface trapping.

A related model ignores the terms p_{nx} and u_{nx} in (11), but retains the meridional pressure gradient, p_{ny}. The essential difference between this dynamics and Ekman dynamics is that now

zonal jets must be in geostrophic balance near the equator. The steady-state solution for each vertical mode is

$$\left.\begin{aligned} v_n &= -\tau_{0n}\frac{\alpha_0}{c}X\sum_{m=0}^{M}\frac{[\eta Y]_m}{\alpha_m^2+A^2/c^6}\phi_m(\eta),\\ u_n &= (c^2/A)\,(c\alpha_0\,\eta v_n+F),\\ p_n &= -(c^4/A)\,\alpha_0\,v_{n\eta}. \end{aligned}\right\} \tag{52}$$

Again, all fields are proportional to X, and radiation plays no role. Yoshida (1959) first found an equatorial v-field like that of (52). It is therefore appropriate to define a single baroclinic mode described by (52) to be in Yoshida balance. An oceanic flow in which all baroclinic modes have this form is a baroclinic Yoshida flow.

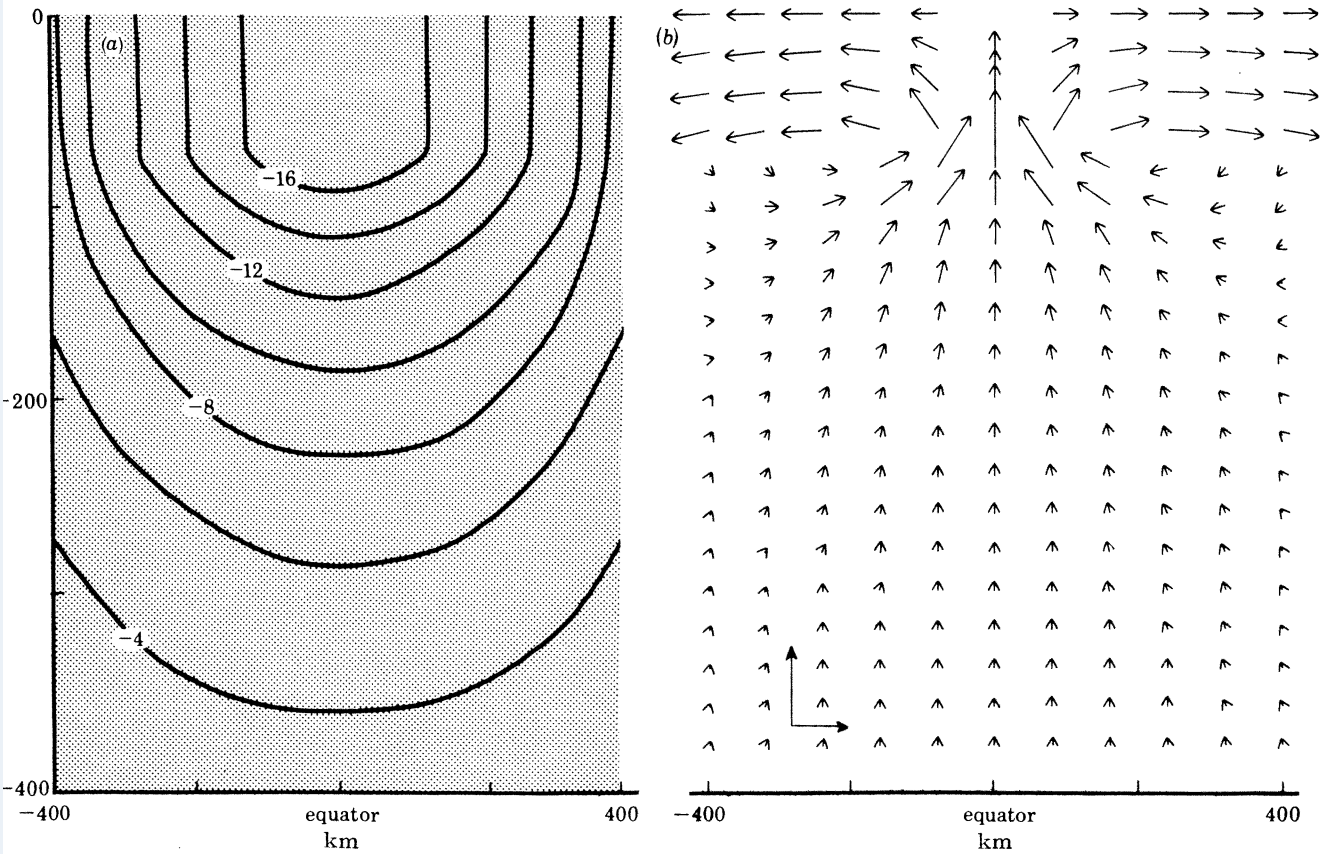

FIGURE 10. Vertical sections of baroclinic Yoshida flow, described by equation (52), showing (*a*) zonal velocity and (*b*) meridional circulation along section 3 of figure 3. The contour interval is 1 km/s. Calibration arrows in the lower left corner of the right panel have amplitudes of 0.005 cm/s and 10 cm/s in the vertical and horizontal directions, respectively. The unrealistic zonal flow field demonstrates the importance of the establishment of baroclinic zonal pressure gradients.

Figure 10 shows a meridional section of a baroclinic Yoshida flow which is comparable to both figures 4*c* and 9. The meridional circulation pattern is much improved over that in figure 9. It closely resembles that of figure 4*c* in both magnitude and structure. The major difference is that in figure 10 the convergence of fluid toward the equator takes place throughout the entire water column, whereas in figure 4*c* the convergence takes place just beneath the surface mixed layer.

The zonal current is still far too large and extends to the ocean bottom; in fact, at the equator it is identical to that of baroclinic Ekman flow. Clearly p_{ny} acts to set a reasonable width scale for the equatorial current system. The zonal pressure gradient, p_{nx}, is essential for limiting the zonal flow and for keeping the flow field confined to the near-surface region.

The reason for the improvement of the Yoshida model compared with the Ekman model is evident in (52) and (51). The equations differ significantly in the structure of the v_n-field. The y-dependence of the Yoshida balance is determined entirely by the Hermite functions, $\phi_m(\eta)$. Therefore, the width scale of the equatorial region is $L = O(\alpha_0^{-1})$, the equatorial Rossby radius of the particular vertical mode, and does not depend on the friction parameter, A. Provided that $\alpha_0^2 \gg A^2/c^6$ (which is true for the first thirty or so vertical modes in the flow field of figure 10), it follows that $v_n = O[F/(c\beta)^{\frac{1}{2}}]$ and $w_n = O(F/c)$, so that the meridional circulation of a baroclinic Yoshida flow is much less dependent on A. The amplitudes of these currents vary like $F/c^{\frac{1}{2}}$ and F/c, which decrease slowly with n. As a result, higher-order modes are more visible in the solution, and the vertical structure of the meridional circulation no longer looks like the first baroclinic mode. At the equator, the zonal flow still has the form $u_n = (c^2/A)\,F$ and suffers the same problems as that of the Ekman model.

A model that illustrates the importance of diffusion in the equatorial ocean ignores all drag terms in (11). In an unbounded ocean the steady solution for each vertical mode is then

$$\left.\begin{aligned} v_n &= -(1/\beta)\,F_y, \\ u_n &= \frac{1}{\beta}\int_{+\infty}^{x} F_y\,\mathrm{d}x + \left\{\frac{1}{2}\frac{\phi_0}{c}\tau_{0n}\,Y_0\int_{-\infty}^{\infty} X\,\mathrm{d}x\right\}, \\ p_n &= \int_{+\infty}^{x} (F - yF_y)\,\mathrm{d}x + \left\{\tfrac{1}{2}\phi_0\,\tau_{0n}\,Y_0\int_{-\infty}^{\infty} X\,\mathrm{d}x\right\}, \end{aligned}\right\} \tag{53}$$

and w_n is identically zero. Note that u_n and p_n are proportional to integrals of X. The dynamics are thus inherently non-local and are intimately related to the presence of equatorially trapped radiation in the model. Except for the terms in curly brackets (53) has the same form as the solutions obtained by Sverdrup (1947) in describing the depth-averaged properties of oceanic flow. It is useful to refer to a single baroclinic mode described by (53) as being in Sverdrup balance, and to an oceanic flow in which all baroclinic modes have this form as a baroclinic Sverdrup flow.

The terms in curly brackets describe an x-independent, geostrophically balanced, zonal jet. This steady jet appears only in an unbounded ocean and was missed by Sverdrup, who solved his equations by requiring the boundary condition that $u = 0$ at an eastern ocean boundary. The correct boundary conditions in the unbounded ocean are actually the radiation conditions described in § 3 of this paper. McCreary (1977, 1978) traces the adjustment of a baroclinic mode to Sverdrup balance from an initial state of rest; the Sverdrup balance, including the equatorial jet, develops only after Rossby and Kelvin waves radiate from the region of the wind. Figure 11*a* (discussed in greater detail below) contrasts the Sverdrup balance in both a bounded and an unbounded ocean.

Baroclinic Sverdrup flows do not have a realistic equatorial current structure. In a bounded ocean, the terms in curly brackets in (53) are absent, and the fields no longer involve c. The sum over all vertical modes can be done explicitly in this case. The result is that all currents are confined entirely to the surface mixed layer. If the wind field has no curl there are no currents; instead baroclinic pressure gradients everywhere balance the wind stress. In an unbounded ocean the terms in curly brackets provide an extra contribution to the flow which at the equator varies

like F/c. Their sum does not converge, but rather has the character of a Dirac δ-function; the Undercurrent appears as an infinitesimally narrow, infinitely strong equatorial jet at the base of the mixed layer. Evidently the vertical diffusion of heat and momentum cannot be neglected in the equatorial ocean.

(*b*) *The effects of radiation*

In equations (11) the size of the drag coefficient, A/c^2, increases rapidly with the value of n. Since c is roughly inversely proportional to n, A/c^2 increases like n^2. As a result, the character of the solutions, (40), also changes markedly with n. Whether the effects of radiation are evident in an individual mode strongly depends on the amplitude of the drag.

The magnitude of A/c^2 affects the solution by specifying the decay rates of waves present in the model. Recall that the solutions all involve terms of the form (41). Suppose that $|k\Delta x| \gg 1$; that is, waves are strongly damped before they can cross the wind patch. In that case, (41) simplifies to

$$\{-\text{const.}\, X/\mathrm{i}k\}\, \mathrm{e}^{\mathrm{i}\sigma t}. \tag{54}$$

If $|k\Delta x| \ll 1$, waves radiate strongly out of the wind patch, and (41) becomes

$$\left\{\text{const.} \int_{\pm\infty}^{x} X\, \mathrm{d}x\right\} \mathrm{e}^{\mathrm{i}(kx+\sigma t)}. \tag{55}$$

When A/c^2 is sufficiently large, $|k\Delta x| \gg 1$ for all waves, and (54) holds for all the integrals in (40). With some algebra, and use of (54), it can be shown that solutions (40) in steady state simplify to the form (52). In other words, the high-order modes of the model, where friction is large, are all in Yoshida balance. When A/c^2 is sufficiently small, $|k_1^m \Delta x| \ll 1$ and $|(\omega/c)\, \Delta x| \ll 1$, but $|k_2^m \Delta x|$ remains greater than 1. With appropriate use of both (54) and (55), the steady-state solutions (40) can be shown to simplify to the form (53). So, low-order modes of the model, where friction is weak and radiation strong, are in Sverdrup balance.

The number of modes that are characterized by Sverdrup balance depends on the size of the friction parameter. In fact, it is possible to choose A so large (unrealistically large) that none of the modes can approach Sverdrup balance. For the solution of figures 4*a–f*, A is set (realistically) so that $|(\omega/c)\, \Delta x| = (A/c^3)\, \Delta x = 1$ for $n = 8$. With this choice $(A/c^3)\, \Delta x = 0.0019$ and 7.02 for $n = 1$ and 15, respectively. Therefore, modes for $n > 8$ tend to be in Yoshida balance, and modes for $n < 8$ tend to be in Sverdrup balance. The oceanic flow generated by the model is neither a Yoshida flow nor a Sverdrup flow, but a combination of both. It can be described as being a Yoshida flow in which, because of the presence of radiation, a finite number of low-order vertical modes tend to be in Sverdrup balance. The modes in Yoshida balance reproduce the meridional circulation pattern associated with the equatorial Ekman pumping process. The modes in Sverdrup balance create zonal baroclinic pressure gradients which balance the driving wind, and so prevent the generation of unrealistically large equatorial zonal jets.

Boundaries are another source of radiation. High-order boundary waves ($n > 8$) decay rapidly and can influence the flow field only near the boundaries themselves. They act to bend equatorial currents into narrow coastal jets. The similarities among the curves of figure 8 are due to the fact that the contributions of high-order modes to the profiles are not affected by ocean boundaries. Low-order waves ($n < 8$) decay weakly and influence the flow everywhere in the ocean basin. Equations (53) indicate how strongly the low-order modes can be altered by boundary radiation. For each mode an equatorial jet, described by the term in curly brackets, extends to the ocean boundaries. Boundary waves cancel this jet at the boundaries and in the interior

PHILOSOPHICAL TRANSACTIONS OF THE ROYAL SOCIETY A MATHEMATICAL, PHYSICAL & ENGINEERING SCIENCES

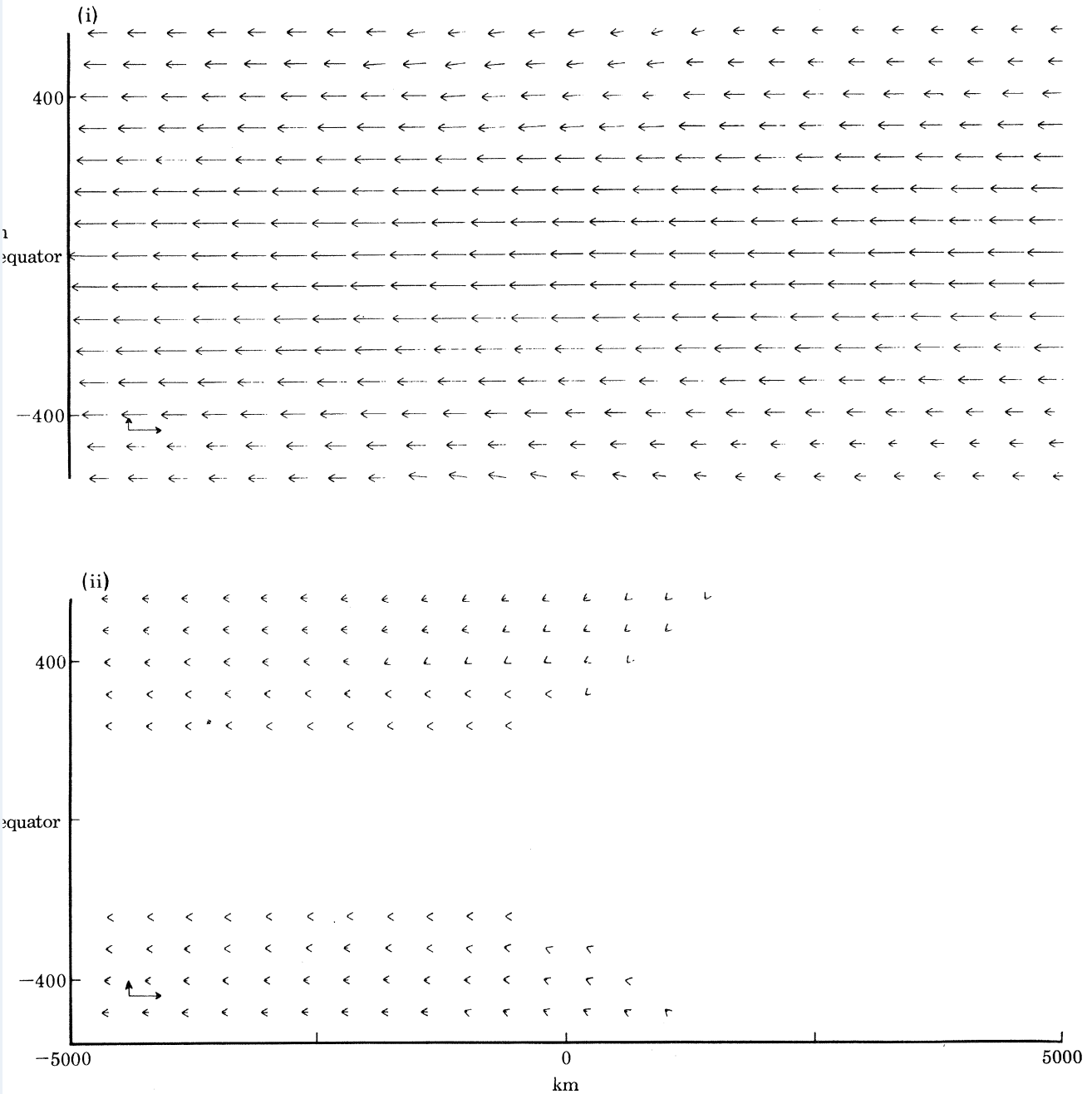

FIGURE 11*a*. The surface velocity fields due to the $n = 1$ mode in both (i) an unbounded ocean and (ii) a bounded ocean. Calibration vectors are 1 cm/s and 10 cm/s in the vertical and horizontal directions, respectively. Because damping is very weak, this mode is in Sverdrup balance, defined by equations (53). An equatorial jet, described by the terms in curly brackets of equations (53), exists in the unbounded ocean, but is not possible in the bounded ocean. The width scale of the jet is the equatorial Rossby radius of the $n = 1$ mode, which here is 380 km.

PHILOSOPHICAL TRANSACTIONS OF THE ROYAL SOCIETY A MATHEMATICAL, PHYSICAL & ENGINEERING SCIENCES

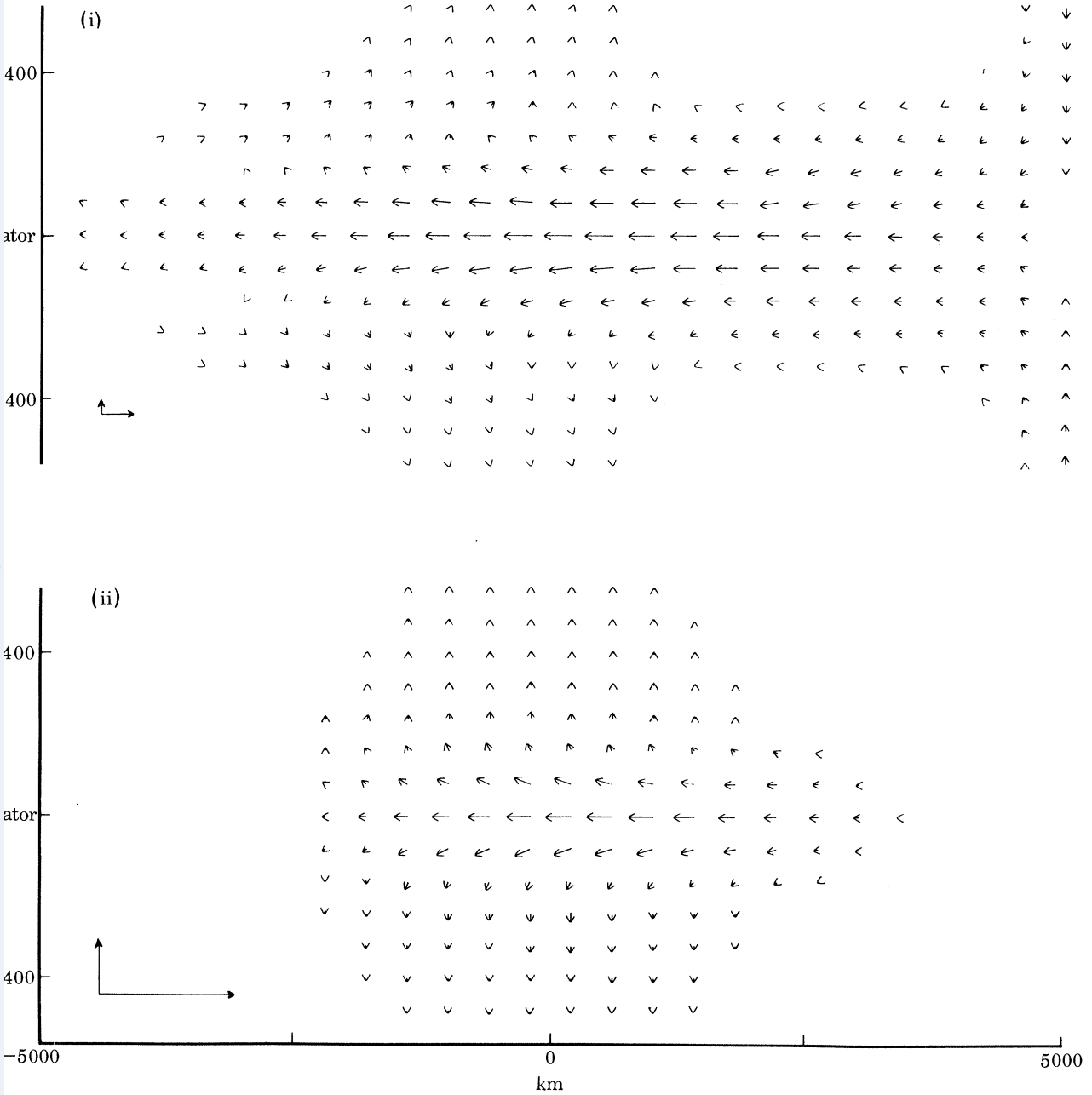

FIGURE 11*b*. The surface velocity fields due to (i) the $n = 8$ mode and (ii) the $n = 15$ mode. Calibration arrows are 1 cm/s and 10 cm/s in the vertical and horizontal directions, respectively. Because damping is strong the $n = 15$ mode is very nearly in Yoshida balance, defined by equations (52). The zonal structure of the flow looks very much like that of the wind field. The $n = 8$ mode has aspects of both the Yoshida and the Sverdrup balances. Damped boundary waves are evident along the eastern boundary. The width scales of the equatorial currents are the equatorial Rossby radii for the $n = 8$ and $n = 15$ modes, which are 134 km and 97 km, respectively.

PHILOSOPHICAL TRANSACTIONS OF THE ROYAL SOCIETY A MATHEMATICAL, PHYSICAL & ENGINEERING SCIENCES

ocean as well. In the inviscid model of equations (53), where the jet is zonally uniform and the boundary waves are undamped, this cancellation is complete. In the present viscid model the boundary waves can only weaken the interior jet, not eliminate it. The differences among the curves of figure 8 are all attributable to whether equatorial jets associated with low-order modes are weakened by the presence of boundaries.

Clearly, higher-order modes play a significant role in this ocean model. Yet previous workers have argued that only the lowest-order vertical modes should be important (Lighthill 1969; McCreary 1977). They assume that a measure of the amplitude of the response of each mode is simply F, the coupling coefficient of the mode to the driving winds. Since F decreases rapidly with n for realistic choices of $\rho_b(z)$, their conclusion follows. The flaw in this argument is that F alone is not an accurate measure of the response of each mode. How rapidly the solution converges with n generally depends in a complicated way on c and other factors as well (Merrill & Geisler 1980). In the present model the effect of the gravest modes on the flow field is inhibited because radiation allows them to adjust to Sverdrup balance; for such modes a measure of the response is either zero or F/c (which decreases slowly with n), depending on whether the ocean is bounded. As a result, higher-order modes are much more visible in the solutions.

The visibility of higher-order modes is apparent in the solution of figures 4*a–f* in that the flows have none of the characteristics associated with the gravest modes. For example, the equatorial Rossby radius, α_0^{-1}, of the $n = 1$ mode is 380 km, but the e-folding width of the model Undercurrent is far smaller than this value. The zero crossing of the $n = 1$ mode occurs at a depth greater than 500 m, but the first zero crossing in the solution occurs just beneath the surface mixed layer. Therefore, the narrow width scale and strong surface trapping of the equatorial currents are directly traceable to the presence of radiation in the model dynamics.

Figures 11*a* and 11*b* illustrate the ideas discussed in this section. They show the surface velocity contributions of individual modes to the solution of figures 4*a–f*. The horizontal structures of the currents vary markedly with n. Damping for the $n = 1$ mode is very small. This mode, then, is virtually in Sverdrup balance. As expected, when boundaries exist there is no equatorial flow. Currents off the equator are caused by the weak wind curl there. Without boundaries there is an additional strong contribution from the equatorial jet. The width of the jet is set by α_0^{-1}, which for this mode is a broad 380 km. Damping for the $n = 15$ mode is strong, and this mode is very nearly in Yoshida balance. An indication of this balance is that the zonal dependence of the flow looks very much like $X(x)$. There is also divergence of fluid from the equator characteristic of Ekman drift there. The e-folding scale of the equatorial current is quite narrow, since for this mode α_0^{-1} is only 97 km. The $n = 8$ mode has aspects of both the Yoshida and Sverdrup balances. The effects of radiation are apparent in that the zonal dependence of the flow does not look much like $X(x)$. Instead, currents extend all the way to the eastern boundary. The flow towards the equator along the boundary indicates the presence of boundary waves. The strength of damping is evident in that the boundary waves decay rapidly back into the ocean interior and do not cancel the equatorial jet. There is divergence of fluid from the equator. For this mode α_0^{-1} is 134 km, and the equatorial jet reflects this scale.

PHILOSOPHICAL TRANSACTIONS OF THE ROYAL SOCIETY A MATHEMATICAL, PHYSICAL & ENGINEERING SCIENCES

6. Summary and discussion

The model studied here can be regarded as an extension of Lighthill's model that allows the diffusion of heat and momentum into the deeper ocean and consequently the existence of non-trivial steady solutions. The equations of motion are also similar to those studied by Stommel (1960). The only difference is that the present model is stratified and so can generate a baroclinic, as well as a barotropic, pressure field. It is perhaps the simplest way to extend Ekman flow to the equator in a stratified ocean.

The response of the model depends on two parameters, $\rho_b(z)$ and ν. The response varies weakly with the shape of the pycnocline below the mixed layer and also with the magnitude of friction in the deeper ocean. The size of friction at the core of the Undercurrent affects the response less than might be expected. For example, the maximum speed of the Undercurrent, U_{max}, varies more weakly with friction than $\nu_{min}^{-\frac{1}{2}}$, whereas in Stommel's homogeneous ocean model U_{max} is inversely proportional to the mixing parameter. The depth of the mixed layer strongly influences the speed of the surface drift, but other properties of the flow to a much lesser degree. The width scale of the equatorial currents is virtually independent of both parameters. In general, the structure of the solutions is insensitive to changes in parameters and thus insensitive to the unconventional parameterization of the diffusion terms, (2).

The expansion of the solution into vertical normal modes provides a very useful way of discussing the dynamics of the model and of understanding many of the properties of the solution. The effects of radiation in the model are evident in that low-order vertical modes can approach Sverdrup balance. Only by means of the radiation of equatorially trapped Rossby and Kelvin waves can a baroclinic mode reach a state of Sverdrup balance. This property weakens the contribution of the low-order modes to the flow field. For example, in a bounded ocean basin the Sverdrup balance is a state of no motion in which a zonal pressure gradient balances the applied wind stress. As a result, higher-order modes are much more visible in the total solution than might be expected. This visibility accounts for the narrow width and surface trapping of the flow field. Higher-order modes tend to be in Yoshida balance, a local dynamics unaffected by radiation. These modes generate the meridional circulation pattern that characterizes equatorial Ekman pumping.

The model is forced by a patch of wind confined to the ocean interior. The wind is steady, westward, and without curl. The model develops a realistic equatorial current structure. Beneath westward surface drift there is an eastward-flowing Equatorial Undercurrent with width, thickness, and magnitude that compare favourably with observation. At greater depths there is a westward Equatorial Intermediate Current. This deeper current exists only in an ocean with meridional boundaries. The meridional circulation pattern closely resembles the flow field suggested by Cromwell (1953). There is a divergence of surface water from the equator, convergence at the core of the Undercurrent, strong upwelling above the current core, and weaker downwelling below. The model baroclinic pressure field closely resembles the observations of Knauss (1966).

The model fails to produce other observed aspects of the equatorial flow field. The Undercurrent necessarily cannot meander in this steady-state model, nor can it develop a secondary ageostrophic Undercurrent (or any velocity shear at all) in the simple mixed layer. The model fails to account for a thick surface mixed layer in the western ocean, and a deep thermostad in the eastern ocean (although the presence of density inversions in this model provides suggestive

hints as to their cause). Model currents are always strongly trapped to the surface, and there is no evidence of large-amplitude stacked zonal jets at the equator. Maximum zonal flow is always concentrated on the equator, and there are no subsurface eastward jets off the equator distinct from the Undercurrent. The model is currently being extended to see if the linear theory can account for some of these phenomena.

The most important result of this paper is that a stratified linear model can generate many of the observed features of the equatorial current system. It is not claimed here that nonlinearities do not play a significant role in equatorial dynamics. Their importance is evident in that the linearized advection of heat allows the development of density inversions. Moreover, without the surface mixed layer the linear surface drift is far too large. Finally, a consistency check (with the aid of figures 4*a–f*) shows that the nonlinear terms uu_x, vu_y, and wu_z are of the same order of magnitude as the linear terms in localized regions of high-velocity gradients. However, the success of the linear model does suggest that nonlinearities are not essential in equatorial dynamics. They apparently act only to modify, not to destroy, the linear solution found here. In conclusion, it is hoped that this paper will facilitate the understanding of more comprehensive, fully nonlinear models of the Undercurrent, like those of Semtner & Holland (1980) and Philander & Pacanowski (1980).

This research was sponsored by the National Science Foundation under grant no. OCE76-00551 through NORPAX, and by the Office of Naval Research under contract no. N00014-C-75-0165. The author is indebted to Mike McPhaden, Michael Spillane, Pijush Kundu, and especially Dennis Moore, for many stimulating and enlightening discussions during the course of this study. Adrian Gill suggested several improvements of an earlier version of this paper. The efforts of Linda Pugh Fann and Jan Witte, who helped to prepare this manuscript for publication, are greatly appreciated.

References

Anderson, D. L. T. & Rowlands, P. B. 1976 The Somali Current response to the Southwest Monsoon: the relative importance of local and remote forcing. *J. mar. Res.* **34**, 395–417.

Arthur, R. S. 1960 A review of the calculation of ocean currents at the equator. *Deep Sea Res.* **6**, 287–297.

Cane, M. A. 1979 The response of an equatorial ocean to simple windstress patterns. I. Model formulation and analytic results. *J. mar. Res.* **37**, 233–252.

Cane, M. A. & Sarachik, E. 1976 Forced baroclinic ocean motions. I. The linear equatorial unbounded case. *J. mar. Res.* **34**, 629–665.

Cane, M. A. & Sarachik, E. 1977 Forced baroclinic ocean motions. II. The linear equatorial bounded case. *J. mar. Res.* **35**, 395–432.

Charney, J. G. 1960 Non-linear theory of a wind-driven homogeneous layer near the equator. *Deep Sea Res.* **6**, 303–310.

Charney, J. G. & Spiegel, S. L. 1971 The structure of wind-driven equatorial currents in homogeneous oceans. *J. phys. Oceanogr.* **1**, 149–160.

Crawford, W. R. 1976 Turbulent energy dissipation in the Atlantic Equatorial Undercurrent. Ph.D. dissertation (149 pp.). University British Columbia, Vancouver, B.C., Canada.

Cromwell, T. 1953 Circulation in a meridional plane in the central equatorial Pacific. *J. mar. Res.* **12**, 196–213.

Cromwell, T., Montgomery, R. B. & Stroup, E. D. 1954 Equatorial Undercurrent in the Pacific revealed by new methods. *Science, Wash.* **119**, 648–649.

Düing, W., Hisard, P., Katz, E., Knauss, J., Meincke, J., Miller, L., Moroshkin, K., Philander, G., Rybnikov, A., Voigt, K., & Weisberg, R. 1975 Meanders and long waves in the equatorial Atlantic. *Nature, Lond.* **257**, 280–284.

Fjeldstad, J. E. 1963 Internal waves of tidal origin. *Geofys. Publr.* **25**, 1–73.

Gill, A. E. 1971 The Equatorial Current in a homogeneous ocean. *Deep Sea Res.* **18**, 421–431.

Gill, A. E. 1972 Models of equatorial currents. *Proc. Symp. Numerical Models Ocean Circulation*, Nat. Acad. Sci., Durham, N.H., 17–20 Oct. 1972.

PHILOSOPHICAL TRANSACTIONS OF THE ROYAL SOCIETY A MATHEMATICAL, PHYSICAL & ENGINEERING SCIENCES

Hisard, P., Merle, J., & Voiturez, B. 1970 The Equatorial Undercurrent at 170° E in March and April, 1967. *J. mar. Res.* **28**, 281–303.

Jones, J. H. 1969 Surfacing of the Pacific Equatorial Undercurrent: direct observation. *Science, Wash.* **163**, 1449–1450.

Knauss, J. A. 1966 Further measurements and observations on the Cromwell Current. *J. mar. Res.* **24**, 205–240.

Lighthill, M. J. 1969 Dynamic response of the Indian Ocean to the onset of the Southwest Monsoon. *Phil. Trans. R. Soc. Lond.* A **265**, 45–93.

Luyten, J. R. & Swallow, J. C. 1976 Equatorial undercurrents. *Deep Sea Res.* **23**, 1005–1007.

McCreary, J. P. 1976 Eastern tropical ocean response to changing wind systems: with applications to El Niño. *J. phys. Oceanogr.* **6**, 632–645.

McCreary, J. P. 1977 Eastern ocean response to changing wind systems. Ph.D. Thesis (156 pp.). University of California at San Diego, Calif.

McCreary, J. P. 1978 Eastern ocean response to changing wind systems. In *Review papers of equatorial oceanography: FINE workshop proceedings* (held in La Jolla, California). Fort Lauderdale, Florida: Nova University Press.

McKee, A. E. 1973 The Equatorial Current in a homogeneous ocean. *Deep Sea Res.* **18**, 421–341.

Merrill, J. T. & Geisler, J. E. 1980 On the relative excitation of vertical modes in tropical ocean initial value problems. (Unpublished manuscript.)

Montgomery, R. B. & Palmén, E. 1940 Contribution to the question of the Equatorial Countercurrent. *J. mar. Res.* **3**, 112–133.

Moore, D. W. & Philander, S. G. H. 1978 Modelling of the tropical ocean circulation. In *The Sea*, vol. 6 (pp. 319–361). New York: Wiley–Interscience.

Moore, D. W., Hisard, P., McCreary, J. P., Merle, J., O'Brien, J. J., Picaut, J., Verstraete, J. & Wunsch, C. 1978 Equatorial adjustment in the eastern Atlantic. *Geophys. Res. Lett.* **5**, 637–640.

Mork, M. 1972 *On the time-dependent motion induced by wind and atmospheric pressure in a continuously stratified ocean of varying depth* (43 pp.). Geophys. Inst., Div. A, Phys. Oceanogr., University of Bergen, Norway.

Philander, S. G. H. 1973 Equatorial Undercurrent: measurements and theories. *Rev. Geophys. Space Phys.* **2**, 513–570.

Philander, S. G. H. & Pacanowski, R. C. 1980 The generation and decay of equatorial currents. *J. geophys. Res.* (To be published.)

Robinson, A. R. 1966 An investigation into the wind as the cause of the Equatorial Undercurrent. *J. mar. Res.* **24**, 179–204.

Semtner, A. J. & Holland, W. R. 1980 Numerical simulation of equatorial ocean circulation. Part 1: a basic case in turbulent equilibrium. *J. phys. Oceanogr.* (To be published.)

Stommel, H. 1960 Wind-drift near the equator. *Deep Sea Res.* **6**, 298–302.

Sverdrup, H. U. 1947 Wind-driven currents in a baroclinic ocean: with application to the equatorial currents of the Eastern Pacific. *Proc. natn. Acad. Sci. U.S.A.* **33**, 318–326.

Tsuchiya, M. 1975 Subsurface countercurrents in the eastern Pacific Ocean. *J. mar. Res. Suppl.* **33**, 145–175.

Veronis, G. 1973 Large-scale ocean circulation. In *Advances in applied mechanics*, vol. 13. New York: Academic Press.

Yoshida, K. 1959 A theory of the Cromwell Current and of the equatorial upwelling. *J. oceanogr. Soc. Japan* **15**, 154–170.

PHILOSOPHICAL TRANSACTIONS OF THE ROYAL SOCIETY A MATHEMATICAL, PHYSICAL & ENGINEERING SCIENCES